

Copyright Warning & Restrictions

The copyright law of the United States (Title 17, United States Code) governs the making of photocopies or other reproductions of copyrighted material.

Under certain conditions specified in the law, libraries and archives are authorized to furnish a photocopy or other reproduction. One of these specified conditions is that the photocopy or reproduction is not to be “used for any purpose other than private study, scholarship, or research.” If a user makes a request for, or later uses, a photocopy or reproduction for purposes in excess of “fair use” that user may be liable for copyright infringement,

This institution reserves the right to refuse to accept a copying order if, in its judgment, fulfillment of the order would involve violation of copyright law.

Please Note: The author retains the copyright while the New Jersey Institute of Technology reserves the right to distribute this thesis or dissertation

Printing note: If you do not wish to print this page, then select “Pages from: first page # to: last page #” on the print dialog screen

The Van Houten library has removed some of the personal information and all signatures from the approval page and biographical sketches of theses and dissertations in order to protect the identity of NJIT graduates and faculty.

ABSTRACT

DIVERSE APPLICATIONS OF NANOSTRUCTURED DIATOM AND ECOTOXICITY OF CARBON NANOTUBES TO ALGA

by
Megha Thakkar

Diatoms are unicellular, photosynthetic microalgae that are widely distributed in fresh and seawater. Frustules or the rigid amorphous silica cell wall of the diatoms have unique porous architecture and high surface area. Recent research shows the potential of nanostructure diatom silica for variety of applications including optics, photonics, bio sensing, filtration, immune precipitation, micro and nanofabrication, protein separation, catalysis and gas sensor. Diatom nanotechnology is not yet fully explored. The unique porous architecture of the diatom was utilized to immobilize various metal oxides like zirconium (Zr) oxide for fluoride removal, iron (Fe) oxide for arsenic removal and bimetallic Fe-Zr oxide for Selenium removal. The composites were characterized and adsorption data were modeled using First and Second order kinetics as well as Langmuir and Freundlich isotherms. The adsorption capacity for fluoride was 15.5 mg/g of diatom zirconium oxide composite, 10 mg/g of arsenite and 12.5 mg/g of arsenate using Diatom iron oxide composite and 227 mg/g of selenate using Diatom Zirconium iron oxide composite. Thus, new generation adsorbents for water treatment were successfully developed.

Further, diatom silica was explored for drug delivery of hydrophobic drug Griseofulvin. Diatom drug composite (DDC) was developed using anti solvent crystallization method. DDC had 30% increased dissolution rate compared with pure

drug. This research for the first time studied the use of laboratory cultured diatom for drug delivery of poorly water soluble drug.

Another area research includes toxicity of carbon nanotubes to green algae *Dunaliella tertiolecta*. With increasing production and use of carbon nanotubes, it is important to study its effects on environment. Algae are present on the surface and are first point of contact, hence it's important to understand the effects and interaction of these materials to algae. Carboxylated functionalized single walled carbon nanotubes (f-SWCNTs) were examined for their toxic effects on marine alga chlorophyte *Dunaliella tertiolecta*. The toxicity was measured based on growth, photosynthetic activities and oxidative stress measured as intracellular glutathione. Physical interactions between the f-SWCNT and alga were also examined. The presence of nanotubes led to a growth inhibition of over 30%, photosynthetic yield decreased by as much as 18% and intracellular glutathione reduction was as high as 95%. The results from f-SWCNTs were somewhat different when compared to our previous study using the same algae and functionalized multi walled carbon nanotubes.

**DIVERSE APPLICATIONS OF NANOSTRUCTURED DIATOM AND
ECOTOXICITY OF CARBON NANOTUBES TO ALGA**

**by
Megha Thakkar**

**A Dissertation
Submitted to the Faculty of
New Jersey Institute of Technology
in Partial Fulfillment of the Requirements for the Degree of
Doctor of Philosophy in Chemistry**

Department of Chemistry and Environmental Science

August 2016

Copyright © 2016 by Megha Thakkar

ALL RIGHTS RESERVED

APPROVAL PAGE

**DIVERSE APPLICATIONS OF NANOSTRUCTURED DIATOM AND
ECOTOXICITY OF CARBON NANOTUBES TO ALGA**

Megha Thakkar

Dr. Somenath Mitra, Dissertation Advisor Date
Distinguished Professor of Chemistry and Environmental Science, NJIT

Dr. Farinas Edgardo, Committee Member Date
Associate Professor and Chairman of Chemistry and Environmental Science, NJIT

Dr. Tamara Gund, Committee Member Date
Professor of Chemistry and Environmental Science, NJIT

Dr. Yong Kim, Committee Member Date
Assistant Professor of Chemistry and Environmental Science, NJIT

Dr. Robert Barat, Committee Member Date
Professor of Chemical, Biological and Pharmaceutical Engineering, NJIT

BIOGRAPHICAL SKETCH

Author: Megha Thakkar
Degree: Doctor of Philosophy
Date: August 2016
Date of Birth: September 7, 1983
Place of Birth: Mumbai, India

Undergraduate and Graduate Education:

- Doctor of Philosophy in Chemistry,
New Jersey Institute of Technology, Newark, NJ, 2016
- Master of Science in Chemistry,
New Jersey Institute of Technology, Newark, NJ, 2010
- Master of Science in Analytical Chemistry,
SNDT University, Mumbai, India, 2006
- Bachelor of Science in Food Science Quality Control,
SNDT University, Mumbai, India, 2004

Major: Chemistry

Selected Publications and Presentations

Thakkar M, Raikar A, Mitra S* 2016, Immobilization of A Nanostructured Hydrophobic Drug on Diatom Mesoporous Silica Backbone by Anti Solvent Precipitation, In preparation.

Thakkar M, Wei L, Mitra S* 2016, Effect on Growth, Photosynthesis and Oxidative Stress on Single Walled Carbon Nanotubes Exposure to Marine Alga *Dunaliella tertiolecta*, Submitted to Aquatic Toxicology

Hua L, Guo L, Thakkar M. et al. 2016, Effects of Anodic Oxidation of a Substoichiometric Titanium Dioxide Reactive Electrochemical Membrane on Algal Cell Destabilization and Lipid Extraction. *Bioresource Technology*, 203:112-7.

- Thakkar M, Randhawa V, Wei L*, Mitra S* 2015, Synthesis of diatom-FeOx composite for remove trace arsenic to meet drinking water standards. *Journal of Colloidal and Interface Science*,457: 169-173.
- Thakkar M, Wu Z, Wei L, Mitra S* 2015, Defluoridation using Diatom-ZrO₂ composite from Algal Biomass. *Journal of Colloidal and Interface Science*,450: 239-245
- Randhawa V, Thakkar M, Wei L* 2014, Effect of algal biomass on its inactivation by hydrogen peroxide: culture study and empirical modeling. *Journal of Applied Phycology*, 26:349-355.
- Randhawa V, Thakkar M, Wei L* 2014, Effect of algal growth phase on *Aureococcus anophagefferens* susceptibility to hydrogen peroxide. *Aquatic Toxicology* 142-143: 230-238
- Thakkar M, Randhawa V, Wei L* 2014, Comparative responses of two species of marine phytoplankton to metolachlor exposure. *Aquatic Toxicology* 126:196-206
- Randhawa V, Thakkar M, Wei L* 2014, Applicability of hydrogen peroxide in brown tide control - culture and microcosm studies. *Plos One* 7(10): e47844
- Wei L*, Thakkar M, Chen Y, Ntim S.A, Mitra S, Zhang X 2010, Cytotoxicity effects of water dispersible oxidized multiwalled carbon nanotubes to marine alga, *Dunaliella tertiolecta*. *Aquatic toxicology* 100: 194-20.
- Thakkar M, Wei L, and Mitra S, Ecotoxicity of carbon nanotubes to algae, *Dunaliella tertiolecta*, 250th American Chemical Society National Meeting, Boston, August 2015.
- Thakkar M, Wei L, and Mitra S, Removal of fluoride using a nanostructured diatom-ZrO₂ composite synthesized from algal biomass, 250th American Chemical Society National Meeting, Boston, August 2015.



Dedicated to the Lotus Feet of Guruhari P.P. Hariprasad Swamiji

And

My Atmiya Family

ACKNOWLEDGMENT

First and foremost; I would like to thank my advisor, Dr. Somenath Mitra for introducing me to the techniques and helping me throughout the research. I am greatly influenced by her kind nature.

It is pleasure to thank Dr. Edgardo Farinas, Dr. Tamara Gund, Dr. Barat Robert and Dr. Yong Kim for being members of my thesis committee. I appreciate their help and feel proud to have great committee members.

Thanks to Dr. Larisa Kristopa, Dr. Yong Pu, and Mr. Yogesh Gandhi, for their support regarding instrumentation and laboratory supplies.

I would like to thank the faculty and staff members of Chemistry and Environmental Science Department, also Library staff for their help and support. It seems impossible to prepare final layout of thesis without the help of Dr. Sortirios Ziavros, the Associate Provost for Graduate Studies and the Associate Director Clarisa Gonzalez Lenahan. I am thankful to them as well as the staff members of the Office of Graduate studies for their support and encouragement.

Special thanks to all lab mates for their continuous assistance during the work. Last but not the least; would like to thank, my Haridham family, P. Premben, P. Sarveshwarben, P. Sarvamben, P. Anamiben, P. Shrutben, P. Shushrutben and P. Shalinben for their blessings, motivation and encouragement.

TABLE OF CONTENTS

Chapter	Page
1 INTRODUCTION.....	1
1.1 Objective	1
1.2 Diatoms.....	
2 SYNTHESIS OF NANOSTRUCTURED DIATOM ZrO ₂ COMPOSITE FOR REMOVAL OF FLUORIDE FROM WATER.....	3
2.1 Synthesis and characterization of Diatom ZrO ₂ composite.....	4
2.2 Defluoridation Studies	5
2.3 Results	6
2.3.1 Characterization of Diatom ZrO ₂ composite	6
2.3.2 Fluoride Removal using Diatom ZrO ₂ Composite.....	11
2.3.3 Effect of Competing Anions.....	18
2.3.4 Desorption and Regeneration.....	18
2.4 Conclusion.....	19
3 SYNTHESIS OF DIATOM FeO _x COMPOSITE FOR REMOVAL OF ARSENIC FROM WATER.....	20
3.1 Synthesis of Diatom FeO _x composite.....	21
3.2 Kinetics and Adsorption Studies.....	22
3.3 Results	22
3.3.1 Characterization of Diatom -FeO _x Composite.....	22
3.3.2 Adsorption Studies	26

TABLE OF CONTENTS
(Continued)

Chapter	Page
3.4 Conclusion.....	33
4 SYNTHESIS OF BIMETALLIC OXIDE ON DIATOM FOR THE REMOVAL OF SELENIUM FROM WATER.....	34
4.1 Synthesis of Bimetallic Diatom Composite	35
4.2 Adsorption Studies	36
4.3 Results.....	37
4.3.1 Characterization of Bimetallic Oxide Diatom Composite.....	37
4.3.2 Selenium Removal Using Bimetallic Diatom Oxide Composite.....	40
4.4 Conclusion.....	45
5 ANTISOLVENT PRECIPITATIVE IMMOBILIZATION OF A NANOSTRUCTURED HYDROPHOBIC DRUG ON SILICA FROM LABORATORY CULTURED DIATOM.....	46
5.1 Preparation of Diatom-Drug Composite.....	48
5.2 Characterization of Drug-Diatom Composite.....	49
5.3 Dissolution Test.....	49
5.4 Results.....	50
5.5 Conclusion.....	56
6 EFFECT ON GROWTH, PHOTOSYNTHESIS AND OXIDATIVE STRESS ON SINGLE WALLED CARBON NANOTUBES EXPOSURE TO MARINE ALGAE DUNALIELLA TERTIOLECTA	57
6.1 Preparation and Characterization of Carbon Materials.....	59
6.2 Algal Strain and Culturing.....	60
6.3 Exposure Studies.....	60

TABLE OF CONTENTS
(Continued)

Chapter	Page
6.4 Culture Analysis.....	61
6.5 Photosynthesis.....	62
6.6 Glutathione.....	62
6.7 Results.....	63
6.7.1 Effect of SWCNTs on Algal Growth.....	64
6.7.2 Aggregation in Presence of SWCNT.....	67
6.7.3 Photosynthesis.....	70
6.7.4 Oxidative Stress.....	72
6.8 Conclusion.....	73
REFERENCES	74

LIST OF TABLES

Table	Page
2.1 Experimental q_e , using different concentration of adsorbent doses (0.01 – 0.15 mg/g) with initial fluoride concentration of 5 mg/L for 24 hours.....	12
2.2 First order and second order kinetics. Initial fluoride concentration was 5 mg/L for 24 hours	14
2.3 Model parameters of Langmuir and Freundlich isotherms for adsorption of fluoride	16
3.1 First Order and Second Order Kinetics of arsenite and arsenate.....	29
3.2 Langmuir, Freundlich and D-R model parameters for diatom-Fe oxide Composite.....	31
4.1 Experimental q_e , using different concentration of adsorbent doses	41
4.2 First Order and Second Order Kinetics	42
4.3 Model parameters of Langmuir and Freundlich isotherms for adsorption of selenium.....	44
6.1 Inhibition in growth rate.....	66
6.2 Induction and relaxation parameters of photosynthesis of cells exposed to 0-20 mg/L of f-SWCNT-A, f- SWCNT filtrate, f-SWCNT-B and carbon black.....	71

LIST OF FIGURES

Figure	Page
2.1 (a) Diatom in suspension, (b) diatom with $ZrOCl_2 \cdot 8H_2O$, (c) suspension after heat treatment at $70^\circ C$ and (d) diatom- ZrO_2 composite.	6
2.2 SEM of (a) diatom, (b) diatom with $ZrOCl_2 \cdot 8H_2O$ and (c) diatom- ZrO_2 composite. TEM of (d) diatom, (e) diatom with $ZrOCl_2 \cdot 8H_2O$ and (f) diatom- ZrO_2 composite. TEM EDX of (g) diatom, (h) diatom treated with $ZrOCl_2 \cdot 8H_2O$ and (i) diatom- ZrO_2 composite.....	8
2.3 FTIR spectra of Diatom (a), diatom – ZrO_2 composite after fluoride adsorption (b), Diatom ZrO_2 composite before fluoride adsorption (c). Left shows spectra between $350-4000\text{ cm}^{-1}$ and right is the expanded view from 350 to 1200 cm^{-1}	10
2.4 TGA of Diatom and Diatom- ZrO_2 composite.....	10
2.5 (a) Fluoride adsorption as a function of time at room temperature. Adsorbent dose was 0.1 g , sample volume was 50 mL , initial fluoride conc. was 5 mg/L , and agitation time was 24 h . (b) Percent fluoride adsorption as a function of pH at room temperature at an adsorbent dose of 0.05 g , sample volume of 50 mL , initial fluoride conc. of 5 mg/L , and agitation time of 24 h	15
3.1 (a) Diatom in suspension, (b) diatom with $FeCl_3 \cdot 8H_2O$, (c) suspension after heat treatment at $70^\circ C$ and (d) diatom- $FeOx$ composite.....	23
3.2 a) SEM of diatom $FeOx$ composite; (b) mapping for Si from diatom and (c) Fe immobilized on diatom surface, (d) TEM of diatom and (e and f) diatom- $FeOx$ composite.....	24
3.3 FTIR spectra of Diatom (a), diatom – Fe oxide composite. Left is between $300-4000\text{ cm}^{-1}$ and right is the expanded view from 300 to 800 cm^{-1}	25
3.4 TGA of diatom-Fe oxide composite.....	26
3.5 Percent adsorption of arsenite (a) and arsenate (b) as a function of time, adsorbent dosage 0.014 g in 50 mL of solution.....	27
3.6 Adsorption capacity of arsenite and arsenate at equilibrium.....	27

LIST OF FIGURES
(Continued)

Figure	Page
4.1 (a) SEM of diatom, (b) diatom bimetallic oxide composite; (c, d) represents mapping for Zr and Fe immobilized on diatom surface. TEM of (e) diatom and (f) diatom bimetallic oxide composite.....	38
4.2 FTIR spectra of Diatom and Diatom bimetallic oxide composite (left), enlarged view of the spectra (right).....	39
4.3 TGA of Bimetallic oxide diatom composite.....	39
4.4 Percent removal of Se (IV) and Se (VI) as a function of time.....	40
4.5 Effect of pH on Se (IV) removal.....	43
5.1 Preparation of diatom drug composite.....	50
5.2 (a) Photograph of vials containing pure drug, diatom and DDC in water (left to right), (b) SEM of pure drug and (c) diatom (d) diatom-drug composite.....	51
5.3 (a) FTIR spectra of DDC, drug, HPMC and Diatom, (b) expanded view of DDC and drug.....	52
5.4 (a) Raman spectra and mapping of the diatom drug composite (b) image of the scanned area, (c) drug distribution in scanned area (2D, blue area corresponds to a non-GF background, green and red area to a high GF concentration) (d) 3D chemical Imaging of the scanned area. Scanning was done at 1699cm^{-1}	54
5.5 Dissolution of pure drug, Drug-HPMC mixture and DDC.....	55
6.1 Scanning Electron Microscopy images of: (a) f-SWCNT-A; (b) f-SWCNT-B and (c) Carbon black.....	64
6.2 In vivo chlorophyll a fluorescence based growth curves of <i>D. tertiolecta</i> exposed to 0, 0.1, 1, 2.5, 5, 10 and 20 mg/L of samples: (a) f-SWCNT-A; (b) filtrate; (c) f-SWCNT-B, and (d) carbon black.....	65
6.3 Particle size measurements using Multisizer coulter counter; (a) f-SWCNT-B without algae; (b) f-SWCNT-B and algae.....	68

LIST OF FIGURES
(Continued)

Figure	Page
6.4 Light microscopy of: (a) <i>D. tertiolecta</i> ; (b-d) differnt cell aggregated with f-SWCNT-B.....	69
6.5 Scanning electron microscopic images of: (a) <i>D. tertiolecta</i> ; (b) cells exposed to f-SWCNT-B showing nanotube aggregates on cell surface.....	70
6.6 Glutathione quantification of <i>D.tertiolecta</i> and cells exposed to 20 mg/L of f-SWCNT-B.....	72

CHAPTER 1

INTRODUCTION

1.1 Objective

The objective of this dissertation is to explore diatom nanotechnology for diverse applications. Specific objectives include (1) immobilize metaloxides on diatom silica and develop diatom-metaloxide composites for water treatment (2) develop a diatom drug composite to increase the solubility of hydrophobic drug. Another objective is to test toxicity of carbon nanotubes to marine alga *Dunaliella tertiolecta*.

For diatom metal oxide composites, nanostructured sorbents like ZrO_2 , FeO_x were immobilized on diatoms to serve as an active ingredient for fluoride, arsenic and selenium removal. The composites developed will serve as a platform technology that can be used in other water remediation applications.

Dissolution of poorly soluble drug was improved by antisolvent precipitation of drug crystals on the diatom surface. Model drug griseofulvin was used in the study.

Effects of carbon nanotubes on marine algae, where high salt concentration leads to aggregation is not well understood. Hence, the effect of carbon nanotubes on photosynthesis activity, growth and oxidative stress using the marine algae *D. tertiolecta* was measured.

1.2 Diatoms

Diatoms are unicellular, photosynthetic microalgae that are widely distributed in fresh and seawater. There are over eleven thousand known species whose size range from $2\mu\text{m}$

to 2 mm and they also have diverse morphology [1]. Frustules or the rigid amorphous silica cell wall of the diatoms have unique porous architecture [2, 3] and their surface area can be as high as 200 m²/g [4]. Recently, they have found a variety of applications including water filtration membrane [5], gas sensor [6], electroluminescent display device [7], lithium battery electrode [7], dye sensitized solar cells [7], biochip [8] and drug delivery [9]. It is possible that the diatoms can serve as hosts for immobilizing active sorbent particles on its surface. The surface of the diatom can have different functionalities such as -COOH, -NH₂, -OH and -SiOH, and different compounds can be immobilized on their surface by interactions with these functional groups [10, 11]. Along with the active sorbent, the support plays an important role which are often dependent on thermal and mechanical behaviour, hydrophobicity and chemical stability [12]. The search for more efficient water treatment media has led to the development of nanostructured adsorbents where metals, metal oxides and ion exchange medium are immobilized on supports that promote nanostructuring [12]. The widely used host materials for nanocomposite include carbonaceous materials like granular activated carbon [13], silica [14-17], cellulose [18, 19], chitosin [20, 21], sand [22, 23] and polymers [24-26]. Some examples include the immobilization of metal oxides on carbon nanotubes for lead, arsenic and fluoride removal [27-29], activated carbon immobilized on carbon nanotubes for chromium removal [13] and carbohydrate and iron oxide on multiwalled carbon nanotubes for zinc removal [30]. In this research, diverse applications have been explored.

CHAPTER 2

SYNTHESIS OF NANOSTRUCTURED DIATOM ZrO_2 COMPOSITE FOR REMOVAL OF FLUORIDE FROM WATER

Removal of fluoride to the recommended level is critical for human health and high fluoride concentration is a global problem. Over 200,000 Americans live in communities where fluoride levels in drinking water are 4 ppm or higher [31]. Fluoride is widely distributed in the geological environment and is generally released into groundwater by slow dissolution of fluoride containing rocks [32]. Anthropogenic activities including glass and ceramic production, semiconductor manufacturing, electroplating, coal fired power generation, beryllium extraction, brick and iron works, aluminum smelters, and phosphate fertilizers also add to high fluoride concentration in drinking water [33]. The Centers of Disease Control has recommended an optimal fluoride concentration of 0.7 ppm. According to the New Jersey Public Water supplies (2011), of the 23 communities sampled, only 5 had fluoride concentration within 0.8 ppm and concentration as high as 3.0 ppm was detected [34]. Reverse osmosis (RO) and adsorption via ion exchange are conventional approaches for defluoridation [35]. These are expensive techniques and there is a great need to develop green materials for water defluoridation. Zirconium oxide is chemically stable, nontoxic and does not dissolve in water. It is insoluble in water at a wide range of pH, hence can be used for defluoridation of ground water, industrial waste and drinking water [36]. Compared to other oxides such as iron and aluminum, there is limited research on zirconium based oxides. Zirconium has shown high adsorption capacity for fluoride and some of the strongest coordination compounds with fluoride are formed with Zirconium [37].

2.1 Synthesis and Characterization of Diatom-ZrO₂ Composite

Diatom *Phaeodactylum tricornutum* was cultured and maintained in Aquil [38] (artificial sea water) using a diurnal Chamber with 12 hour day/night cycles at 19°C±1°C. The diatom culture was flocculated with 0.8mM ZrOCl₂.8H₂O (purchased from Sigma Aldrich) at pH 9. One molar NaOH was used to adjust the pH.

After flocculation, the culture was conditioned overnight with shaking (150 rpm, 2880 VWR orbital shaker). The resulting diatom-ZrO₂ mixture was separated by gravitational settling and membrane filtration (< 5 psi, 0.2 µm PTFE filter), and was washed with 500 mL Milli-Q water. The resulting slurry was transferred to 50-mL centrifuge tube and thermally treated at 70°C in an oven for 10 h. Then, it was treated with 10 mL of concentrated H₂SO₄ and heated for 2 hrs at 200°C, vacuum filtered using 0.2µm filter, washed with Milli-Q water to neutral pH and then dried at 200°C in a vacuum oven. Five hundred milligram of the product was made using 40 L of *Phaeodactylum tricornutum* culture.

The diatom- ZrO₂ composite was characterized using transmission electron (HRTEM) equipped with Energy Dispersive X-ray Spectrometer (EDX), scanning electron microscope (SEM, LEO 1530 VP), Thermogravimetric Analyzer (TGA using Pyris 1 from PerkinElmer Inc), BET surface area analyzer (Quantachrome Autosorb-1), FTIR (IR Affinity -1, Shimadzu) and dynamic laser scattering (ZetasizerNano by Malvern Instruments) for particle size and zeta potential measurements.

2.2 Defluoridation Studies

The fluoride adsorption capacity of the diatom-ZrO₂ composite was investigated as follows. A fluoride ion stock solution at a concentration of 1000 mg/L was prepared and other standards were made by subsequent dilution. An Orion potentiometer (Model SA 720) with a omega fluoride ion selective electrode (FISE) in combination with a single-junction Ag | AgCl | Cl⁻ reference electrode potentiometer was used to measure aqueous fluoride ion concentration. A linear calibration curve in the range 0.01 to 100 mg/L was used for quantification. The sensitivity, accuracy and reproducibility of the procedure were assessed using sodium fluoride standards. The fluoride solutions and the adsorbents were thoroughly mixed at a speed of 200rpm on a Remi shaker. The mixture was filtered through a 0.2µm membrane syringe filter. The filtrates of fluoride adsorbed were immediately analyzed by the Fluoride ion selective electrode.

The kinetics of adsorption was performed as follows. A 50 milliliter of 5 mg/L of fluoride solution was contacted with 0.01 g and 0.1 g of adsorbent in polycarbonate bottles and the samples were collected at 3, 10 and 15 min. followed by 1, 3, 5, 7 and 24 hrs. Defluoridation experiments were carried out in duplicate and the relative standard deviation was found to be below 7% during at initial 3 minutes of exposure and less than 3% after equilibration. Adsorption was studied at pH 2, 4, 6 and 8 using 50 milliliter of 5 mg/L fluoride solution that was contacted with 0.05 g of adsorbent for 24 h. The adsorption capacity (q_e) and adsorption isotherms were obtained by varying the mass of adsorbent from 0.01 to

0.15 g with 50 mL of 5 mg/L fluoride containing water at pH 6 and the samples were collected at 0, 7 and 24 hours.

The effect of potentially competing oxyions, namely silicates, bicarbonate and nitrates were evaluated. The experiments were conducted at room temperature and at pH 6 at a fluoride concentration of 5 mg/l. The concentrations of silicates, bicarbonate and nitrates ions were 1, 2 and 1 mM, respectively. Desorption of fluoride from the spent diatom-ZrO₂ composite was carried out using 1 M NaCl and 0.1M NaOH solution. After fluoride adsorption, the composite was washed with 1M NaCl, followed by distilled water and 0.1 M NaOH.

2.3 Results

2.3.1 Characterization of Diatom- ZrO₂ Composite

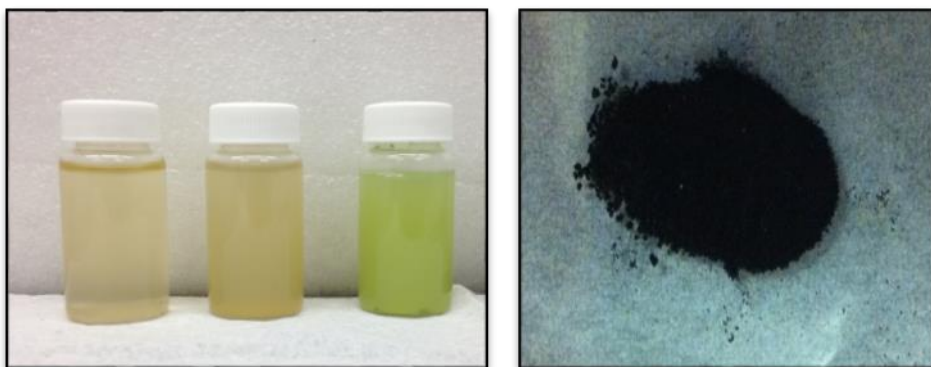


Figure 2.1 (a) Diatom in suspension, (b) diatom with ZrOCl₂·8H₂O, (c) suspension after heat treatment at 70°C and (d) diatom-ZrO₂ composite.

The photographs of diatom-ZrO₂ composite synthesis are presented in Figure 2.1. After adding ZrOCl₂·8H₂O and NaOH to the diatom, ZrO₂ was precipitated on the diatom surface via chemical interactions with diatom functional groups like -COOH, -NH₂, -OH

and -SiOH . This was enhanced by heat treatment at 70°C for 10 h. Furthermore, H_2SO_4 treatment decomposed all the organic matter leaving algal core with ZrO_2 on its surface. Mesoporous Zirconia can be obtained by contacting amorphous hydrous Zirconia obtained by alkaline hydrolysis with sulfuric acid followed by calcinations [39].

Algae present on surface waters are the dominant primary producers in marine ecosystems [40]. They form a base for the oceanic food web and serve as major components of the global carbon and biogeochemical cycles. Algal populations are affected by anthropogenic pollutants flowing into ecosystems and are important indicators for environment pollution. Nanoparticles with their high surface area and abundant reactive sites can be significant sources of environmental pollution [41]. Algae whose cell walls act as primary sites for interaction with nanoparticles have been effectively used as model organisms to assess nanoparticle ecotoxicity [42].

A large percentage of all drug molecules developed in pharmaceutical industry are hydrophobic and consequently have low aqueous solubility as well as bioavailability [43]. Dissolution is a limiting factor in their *in vivo* performance and increasing this is a major challenge [44]. Surface area enhancement via nanostructuring has been a common approach to increasing the dissolution rate [45]. Nano drug particles have been synthesized via top-down approaches such as milling or high pressure homogenization as well as by crystallization techniques [46]. Other approaches to enhance dissolution includes complexation with cyclodextrin [47], microemulsion formation [48], encapsulation in polymer films [49] and deformable membrane vesicles[50].

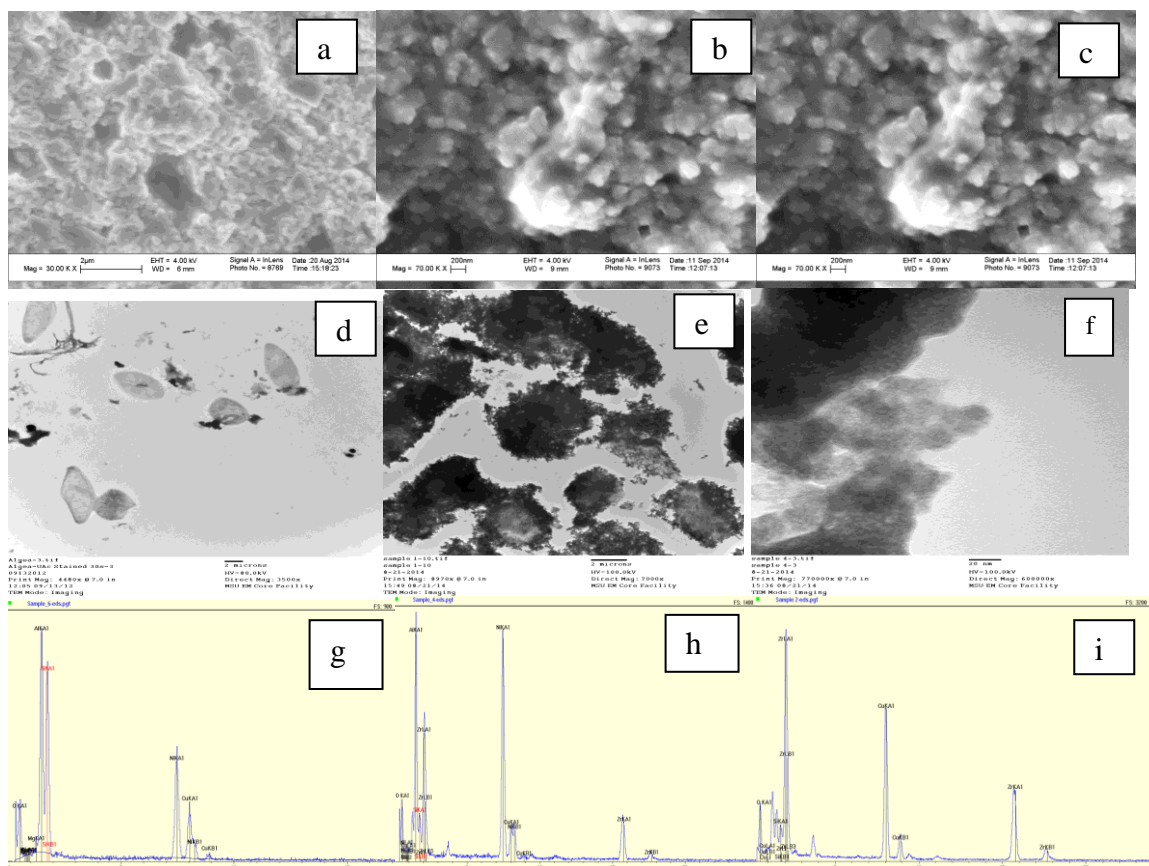


Figure 2.2 SEM of (a) diatom, (b) diatom with $ZrOCl_2 \cdot 8H_2O$ and (c) diatom- ZrO_2 composite. TEM of (d) diatom, (e) diatom with $ZrOCl_2 \cdot 8H_2O$ and (f) diatom- ZrO_2 composite. TEM EDX of (g) diatom, (h) diatom treated with $ZrOCl_2 \cdot 8H_2O$ and (i) diatom- ZrO_2 composite.

The diatom was contacted with $ZrOCl_2 \cdot 8H_2O$ to take advantage of the biosilica structure in their native architecture. Under alkaline pH, the ZrO_2 precipitated on the diatom surface. The presence of ZrO_2 particles on diatom surface was studied at various steps in the process using SEM and TEM fitted with EDX. Figure 2.2a shows SEM of the original diatom, 2.2b is diatom contacted with $ZrOCl_2 \cdot 8H_2O$ and 2.2c is diatom- ZrO_2 composite. Similarly, figure 2.2d shows TEM image of the diatom, 2.2e diatom contacted with $ZrOCl_2 \cdot 8H_2O$ and Figure 2.2f diatom- ZrO_2 composite. SEM and TEM images showed that the original diatom was reduced to porous nano biosilica. Also, Figures 2.2c

and 2.2f show that heat and acid treatment allowed precipitated Zr to form a composite with porous nano biosilica. EDX analysis using TEM confirmed presence of Si in the diatom, and Si and Zr from diatom-ZrO₂ composite. The TEM-EDX analysis showed comparatively higher Zr content than Si before and after acid treatment. The ratio of Si:Zr before acid treatment was 1:4.5 and after acid treatment was 1:4.0.

The specific surface area of diatom- ZrO₂ composite based on BET measurements was found to be 140 m²/g and pore width was 9.7 Å. Development of diatom-ZrO₂ composite using hydrogen peroxide treatment instead of sulphuric acid was also carried out. However, the surface area of the composite was around 70 m²/g and had comparatively less adsorption capacity. The sulphuric acid facilitated the formation of mesoporous sulphated Zirconia with high surface area [51]. The particle size of diatom-ZrO₂ agglomerates in water were found to be 80 nm ± 2 nm (by DLS measurements) while zeta potential was -30. This indicated that the particles were quite stable in an aqueous suspension. The carboxylic and other polar groups on the surface contributed to the stability of the particles. The size of diatom *Phaeodactylum tricornutum* was around 3.5µm [52], heat and acid treatment reduced the size (Figures 2.2c and 2.2f).

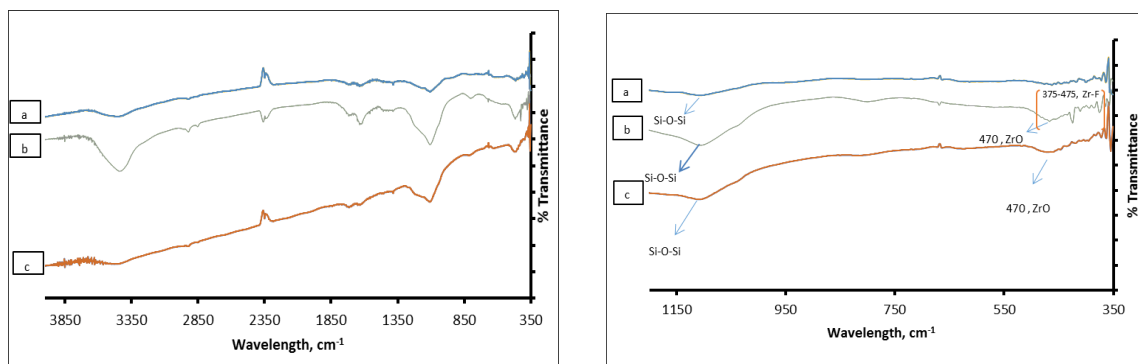


Figure 2.3 FTIR spectra of Diatom (a), diatom – ZrO₂ composite after fluoride adsorption (b), Diatom ZrO₂ composite before fluoride adsorption (c). Left shows spectra between 350-4000 cm⁻¹ and right is the expanded view from 350 to 1200 cm⁻¹.

The FTIR spectrum (Figure 2.3) was used to confirm the functional groups. The observed peak at 470 cm⁻¹ was attributed to Zr-O vibration, which confirmed the ZrO₂ structure [53]. The Zr-F stretch was between 375 and 475 cm⁻¹[54]. All the three spectra showed peaks at 1108 and between 3300 cm⁻¹ to 3500 cm⁻¹. These were due to stretching of siloxane (Si-O-Si) and free silanols group (Si-OH) [55].

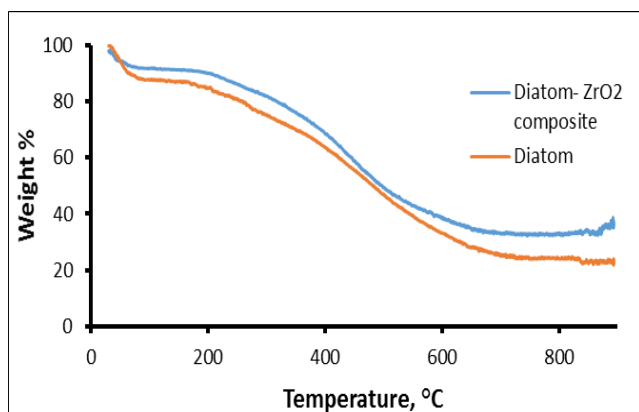


Figure 2.4 TGA of Diatom and Diatom-ZrO₂ composite.

TGA was used to test the thermal stability of the diatom-ZrO₂ composite (figure 2.4). The weight loss below 120 °C was attributed to the removal of

physisorbed water while the loss between 120-300 °C was due to chemisorbed water [56]. In the 300-400 °C range, the weight loss was from the oxidation and decomposition of mercaptopropyl or aminopropyl groups on diatom surface. The broad exothermic weight loss in the range of 400-600 °C was due to the decomposition of strongly tethered organosilanes and dehydration of silanol groups, and the weight reduction between 400–800 °C was due to the dehydroxylation of the silica surface. [57, 58]. TGA curve indicated that Diatom-ZrO₂ composite exhibited good thermal stability. It is worth noting that the observed weight loss (19%) below 300 °C was mainly ascribed to the evaporation of water. In the case of the diatom, only 23% of the mass remained as residue beyond 600 °C, and the residue was 38% in case of the diatom- ZrO₂ composite.

2.3.2 Fluoride Removal using Diatom-ZrO₂ Composite

It was observed that no fluoride was adsorbed on the pure diatom, but diatom-ZrO₂ composite was effective in removing fluoride from water. Fluoride uptake by diatom-ZrO₂ composite was studied as a function of time and is presented in Fig. 5a. Fluoride sorption increased exponentially as a function of contact time until equilibrium was reached. Fluoride uptake reached 79% of the equilibrium value within the first 15 minutes, indicating high rate of adsorption. The slow uptake after the initial period was attributed to diffusion controlled processes. Natural water tends to be acidic due to dissolved CO₂ with typical pH between 5.5 to 6. The diatom- ZrO₂ composite was also acidic in nature due to carboxylation during the acid treatment; however, the addition of the diatom-ZrO₂ did not change the pH of the water.

The amount of fluoride adsorbed was calculated using the following equation:

$$q_e = \frac{(C_0 - C_e) V}{m} \quad (2.1)$$

Where, C_0 and C_e (mg/L) are the liquid-phase concentrations of fluoride at initial and equilibrium concentrations, respectively. V is the volume of solution in (L) and m is the mass of the adsorbent used (g). Adsorbent dosage is an important parameter because this determines the capacity of an adsorbent. It was observed that at equilibrium, the percentage removal increased with the increase in the adsorbent concentration while the adsorption capacity q_e decreased.

Table 2. 1 Experimental q_e , using Different Concentration of Adsorbent Doses (0.01 – 0.15 mg/g) with Initial Fluoride Concentration of 5 mg/L for 24 Hours

Initial Adsorbent Concentration (g)	Experimental q_e mg/g	% Removal
0.010	9.40	37.40
0.025	6.07	48.23
0.050	4.29	79.48
0.100	2.34	92.49
0.150	1.58	93.46

Table 2.1 presents the q_e at different adsorbent dosage. It was seen that the initial adsorbent dose affects the adsorption capacity; q_e dropped from 9.40 mg/g for 0.01 g of adsorbent to 1.58 mg/g for 0.15 g.

The kinetics of fluoride uptake was studied using Langereen [59] as well as Ho and Mckay kinetic models [60]. The former models the rate of adsorption of pollutants based on pseudo first equation to describe the kinetics of liquid-solid phase adsorption [61].

$$\log (q_e - q_t) = \log q_e - \frac{k_1}{2.303} t \quad (2.2)$$

The rate constant k_1 was calculated from a linear plot of $\log (q_e - q_t)$ versus t , where q_e and q_t are the sorption capacity (mg/g) of the adsorbent at equilibrium and at time t (h^{-1}), and K^1 is the rate constant of pseudo first order. The second order equation from Ho and Mckay is based on the assumption that adsorption may be second order and the rate limiting step may be from chemical adsorption involving exchange of valence electrons [62].

$$\frac{t}{q_t} = \frac{1}{k_2 q_e^2} + \frac{t}{q_e} \quad (2.3)$$

The rate constant K_2 was calculated from a linear plot of t/q_t versus t . Here k_2 is the pseudo-second order sorption rate constant (g/h/mg) and t is time (h^{-1}). The applicability of first and second order model was tested for adsorption of fluoride on diatom-ZrO₂. Table 2.1 presents the first and second order kinetics data, the best fit was selected based on the linear regression coefficient R^2 . The

models were fitted with the experimental data at different adsorbent dosage (0.01 and 0.1 g). Ho and Mac Kay second order equation was found to be a better fit (r^2 0.999) as compared with the first order equation. The experimental and calculated q_e were compared and closest match was seen using second order model at 0.1 g adsorbent dosage.

Table 2.2 First Order and Second Order Kinetics. Initial Fluoride Concentration was 5 mg/L for 24 Hours

Model	Concentration (g)	Experimental q_e (mg/g)	Calculated q_e (mg/g)	K	R^2
First Order	0.010	9.40	7.15	0.0868	0.9296
Second Order			11.32	0.0177	0.9999
First Order	0.100	2.36	1.85	0.3454	0.8691
Second Order			2.36	0.0089	0.9999

The adsorption rate obtained from first and second order kinetic models are given in Table 2.2. For first order, a larger adsorption rate constant usually represents quicker adsorption whereas for second order, a lower value of k represents faster adsorption. It was seen that the data with 0.1 g sorbent dosage had higher adsorption rate. This may be due to the availability of large number of binding sites. It is worth mentioning that the sorption capacity is comparable to those reported before. For example q_e of 4.95 mg/g was reported for Zr impregnated cellulose [63], q_e of 4.72 mg/g using carbon nanotube Zirconium dioxide hybrid [64] and q_e of 1.27 mg/g was reported for direct sorption on algal biomass [12].

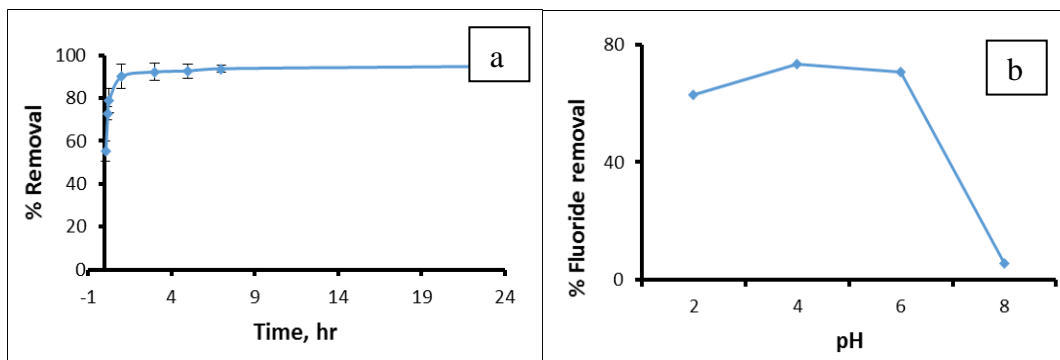


Figure 2.5 (a) Fluoride adsorption as a function of time at room temperature. Adsorbent dose was 0.1 g, sample volume was 50 mL, initial fluoride conc. was 5 mg/L, and agitation time was 24 h. (b) Percent fluoride adsorption as a function of pH at room temperature at an adsorbent dose of 0.05 g, sample volume of 50 mL, initial fluoride conc. of 5 mg/L, and agitation time of 24 h.

The effect of pH was studied at 2, 4, 6, and 8 (Figure 2.5b). The variation in pH in the range of 2 to 6 didn't show much effect on percent adsorption. With increase in pH from 6 to 8, the adsorption capacity decreased. At low pH conditions, the H_3O^+ ion concentration was optimum to make the surface of diatom- ZrO_2 positively charged and hence accessible for fluoride ions. With an increase in pH, especially in alkaline medium, the fluoride uptake was reduced due to the competition with OH^- , which also had high affinity for the zirconium ion.

Langmuir [65] and Freundlich [66] isotherms provided an insight into the surface coverage via physisorption or chemisorption. Langmuir Isotherm best describes the Chemisorption process. The adsorption involves the attachment of monolayer of molecules on the surface. The linear form of Langmuir adsorption isotherm, which involves a plot of $1/q_e$ vs. $1/C_e$, is represented as:

$$\frac{1}{q_e} = \frac{1}{q_m} + \frac{1}{bq_m C_e} \quad (2.4)$$

Here, q_m (mg/g) is the maximum sorption capacity of the sorbent; C_e (mg/L) is the equilibrium fluoride ion concentration and Langmuir constant b (L/mg) is indirectly related to the enthalpy of adsorption. The essential features of Langmuir adsorption parameters can be used to predict the affinity between the sorbent and the sorbate using the dimensionless separation factor which is expressed as follows:

$$R_L = \frac{1}{1 + bC_0} \quad (2.5)$$

Where b is Langmuir constant and C_0 is initial concentration. R_L indicates the nature of adsorption (R_L between 0 to 1 is considered favourable, $R_L < 1$ is unfavourable and $R_L = 0$ is reversible) [67, 68].

Table 2.3 Model Parameters of Langmuir and Freundlich Isotherms for Adsorption of Fluoride

<i>Adsorbent</i>	Langmuir parameters			Freundlich parameters		
	q_m (mg/g)	b (L/mg)	R^2	k_f (mg/g)	n	R^2
<i>Diatom-ZrO₂</i>	15.53	0.48	0.956	4.4	0.64	0.957
q_m - the maximum sorption capacity of the sorbent; b - Langmuir constant; k_f - Freundlich constant; R^2 - correlation coefficient.						

The Langmuir parameters are presented in Table 2.3. The correlation coefficient R^2 values for the Langmuir model were 0.956, demonstrating high degree of correlation. The maximum adsorption capacity of fluoride on the composite was 15.5 mg/g at pH 6. The Langmuir constant b , the ratio of adsorption rate constant to desorption rate constant is an indication of affinity of the sorbent material towards fluoride. Since R_L was less than 1, the adsorption was considered favourable. Hence Langmuir model effectively explained the fluoride uptake by diatom-ZrO₂.

Freundlich adsorption was also tested. In its linearized form, the Freundlich isotherm involves a plot of $\log q_e$ and $\log C_e$:

$$\log q_e = \log k_f + n \log C_e \quad (2.6)$$

The values for $\log k_f$ and n were obtained as the intercept and slope, respectively (Table 2.3). A measure of adsorption capacity and adsorption intensity was provided by the Freundlich constants k_f (mg g⁻¹) and $1/n$, respectively. Here, n was an indicator of the degree of nonlinearity between water concentration and sorption ($n=1$ denotes linear adsorption, $n < 1$ a chemisorption and if $n > 1$ implies physisorption [69]. The bond energy increases proportionally with surface density for $n < 1$ and vice versa for $n > 1$. A value of n being equal 0.64 implied that the adsorption was a chemical process, and that the bond energy increased with surface coverage [66]. The correlation coefficient, R^2 , was 0.95.

Based on the second order kinetics, Langmuir model and Freundlich model, the adsorption appeared to be via a chemical process. Zirconia is known to have high affinity for fluoride and the defluoridation could occur due to several possible mechanisms published before and not repeated for brevity [64]. The Zirconia based Lewis acid sites also acted as sorption sites of the fluoride ions which is a Lewis base. Other possible mechanisms include ion exchange, non-covalent H-bonding interactions as well as covalent ligand exchange.

2.3.3 Effect of Competing Anions

The influences of coexisting anions namely silicates, nitrates and bicarbonate (1, 2, 1 mM, respectively) on the fluoride uptake was investigated. Presence of 2 mM nitrates had negligible effect on fluoride adsorption. This suggests that the binding affinity of nitrates for zirconia was weaker than fluoride. However, no adsorption was seen in presence of 1mM bicarbonate and silicate ions. High concentration of bicarbonate ions may compete with fluoride ions via ion exchange leading to lower fluoride removal. Results are comparable to previously published studies [70-72]. Similar data has been published by our group using a carbon nanotube zirconium dioxide hybrid [64].

2.3.4 Desorption and Regeneration

Desorption of fluoride and regeneration of diatom- ZrO_2 was studied by monitoring the effluent washes from a fluoride sorbed diatom- ZrO_2 composite. 0.1 g of adsorbent was contacted with 50 mL of 5 mg/L of fluoride solution. After 24 hours of exposure, the solution was vacuum filtered using 0.2 μ m filter and washed with 1 M NaCl followed by distilled water and 0.1 M NaOH solutions.

Brine wash resulted only in small amounts of fluoride desorption indicating that only a small fraction of F^- ions is held by ion-exchange/electrostatic forces. A nearly complete removal of adsorbed fluoride was achieved by alkali wash which overcame all interactions of the sorbent with fluoride through a dominating competition for surface active sites. In short, the fluoridated diatom- ZrO_2 composite could be regenerated relatively easily by treating with an alkaline solution (e.g., 0.1 M NaOH). Sodium hydroxide quantitatively desorbed all bound fluoride without damaging the diatom- ZrO_2 composite which could be reused after washing it with 0.1 M H_2SO_4 acid followed by distilled water till neutral pH. Two successive regenerations showed more than 90% removal efficiency similar to the first set of defluoridation experiments.

2.4 Conclusion

Diatom offers unique architecture with excellent mechanical strength. This chapter highlights the potential of diatom as the host for immobilizing nanomaterials to form composite. Zirconium was successfully immobilized on diatom surface and a nanocomposite with high surface area was synthesized. This was achieved by precipitating ZrO_2 on the diatom and then oxidizing the organic mass. Maximum adsorption capacity of 15.0 mg/g adsorbent was calculated using the Langmuir adsorption isotherm. A variation in pH within the 2 to 6 did not alter the adsorption capacity, but a significant reduction in capacity was seen at pH 8.

CHAPTER 3

SYNTHESIS OF NANOSTRUCTURED DIATOM FeO_x COMPOSITE FOR REMOVAL OF ARSENIC FROM WATER

Arsenic affects millions of people across the globe and is a priority for the World Health Organization (WHO) [73-76]. The sources of arsenic in ground water are primarily associated with oxidative weathering, but anthropogenic activities such as industrial effluents from metal processing and pesticides manufacturing also contribute to arsenic contamination [77]. The WHO guideline calls for a maximum drinking water arsenic concentration of 10 ppb and the US-EPA plans to lower the standards to 5 ppb [78]. Arsenic can exist as arsenite (As III) and in oxidized conditions as arsenate (As V). Several studies have concluded that the former is more toxic [79] and is more mobile because it is less strongly adsorbed on most mineral surfaces [80]. Current arsenic removal methods include adsorption, co-precipitation, ion exchange, and bioremediation. The main sorbents of choice for As removal are oxides and hydroxides of iron and aluminum [81], carbon [82], and polymeric materials [73]. Among these, the iron oxides (FeO_x) have shown promising results for both arsenite and arsenate [83].

Diatoms are unicellular, photosynthetic microalgae that are widely distributed in fresh and seawater. Frustules or the rigid amorphous silica cell wall of the diatoms have unique porous architecture [2, 3] and their surface area can be as high as 200 m²/g [4]. The surface of the diatom also have different functional groups such as COOH, -NH₂, -OH and SiOH which can be used to attach other functionalities. The objective of this research was to develop nanostructured

sorbents by immobilizing ferric oxide on diatoms to serve as active ingredient for arsenic removal. The diatom FeOx composite developed here can potentially serve as a platform technology that can be used in other water remediation application

3.1 Synthesis of Diatom-FeOx Composite

Diatom *Phyaedactylum tricornutum* was cultured and maintained in Aquil (artificial sea water) using a Diurnal Chamber with 12:12 day: night cycle at $19^{\circ}\text{C}\pm 1^{\circ}\text{C}$. The diatom culture was flocculated with 0.4 mM $\text{FeCl}_3\cdot 8\text{H}_2\text{O}$ (purchased from Sigma Aldrich) at pH 9. One molar NaOH was used to adjust the pH. After flocculation, the diatom culture was conditioned overnight with shaking (150 rpm, 2880 VWR orbital shaker). The resulting diatom- FeOx mixture was separated by gravitational settling and membrane filtration (< 5 psi, 0.2 μm PTFE filter), and washed with 500 mL Milli-Q water. The resulting slurry was transferred to 50-mL centrifuge tube and thermally treated at 70°C in an oven for 6 h. This was followed by drying overnight in a speedvac (Savant AS160) under vacuum. It was further bleached using excess 30% H_2O_2 in a beaker for 40 min, washed until a neutral pH was obtained and then dried at 70°C . This decomposed the biological matter in the diatom. The diatom-FeOx composite was characterized using transmission electron (HRTEM), scanning electron microscope (SEM, LEO 1530 VP) equipped with Energy dispersive X-ray Spectrometer (EDX), BET surface area analyzer (Quantachrome Autosorb-1), Thermogravimetric Analyzer (TGA using Pyris 1 from PerkinElmer Inc) and FTIR (IRAffinity -1, Shimadzu)

3.2 Kinetics and Adsorption Studies

100 ml of different concentrations of arsenite (61, 89,133, 193 and 299 ppb) and arsenate (68, 103, 151, 213 and 334 ppb) were contacted with 0.014 g of diatom-FeOx and placed in the shaker at 250 rpm. 5 mL aliquot was withdrawn at different time intervals, filtered using 0.2 μm membrane filter and residual arsenic in the media was quantified using Agilent 7500 ICP-MS. All standards were prepared from multi-element solution 2A, 10mg/L (Spex Certiprep) with addition of internal standard mix (Li6, Ge, Y, In, Tb, Bi). Multi-element instrument calibration standard 1 and 20 mg/L (Spex Certiprep) was used for the verification of calibration.

3.3 Results

3.3.1 Characterization of Diatom-FeOx Composite

Amorphous FeOOH can be prepared by mixing iron (III) salt and a caustic solution such as NaOH according to:

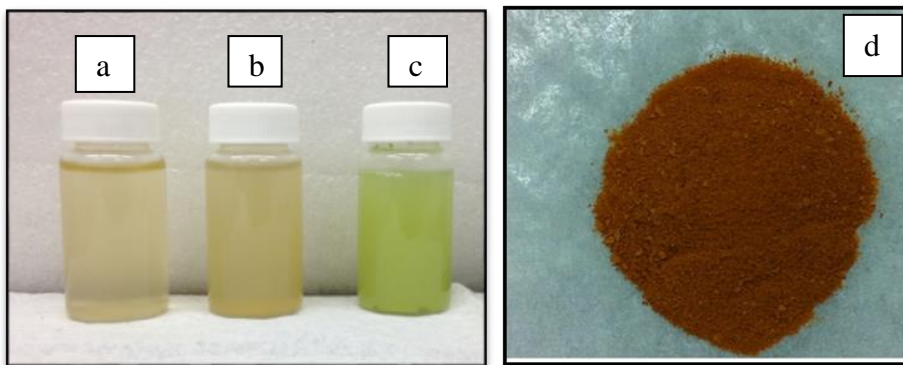
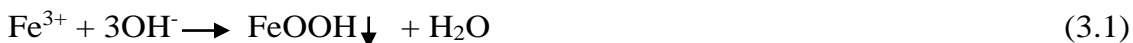


Figure 3.1 (a) Diatom in suspension, (b) diatom with $\text{FeCl}_3 \cdot 8\text{H}_2\text{O}$, (c) suspension after heat treatment at 70°C and (d) diatom-FeOx composite.

Diatoms were contacted with $\text{FeCl}_3 \cdot 8\text{H}_2\text{O}$ to take advantage of the biosilica structure in their native architecture. Under alkaline pH, iron oxide precipitated on the diatom surface and the composite was formed by heating which was followed by hydrogen peroxide treatment [83-85]. The photographs of diatom-FeOx composite are presented in Figure 3.1.

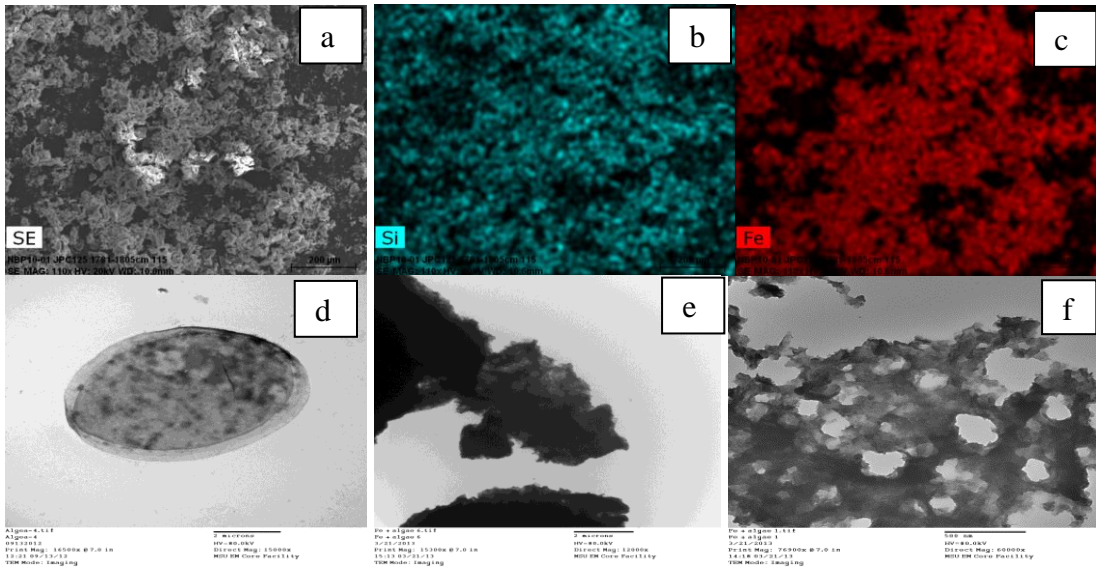


Figure 3.2 (a) SEM of diatom FeOx composite; (b) mapping for Si from diatom and (c) Fe immobilized on diatom surface, (d) TEM of diatom and (e and f) diatom-FeOx composite.

SEM with EDX (Figures 3.2a, 3.2b, 3.2c) showed the presence 1.75% Si from the diatom along with 35% Fe. EDX mapping confirmed uniform distribution of Fe on diatom surface. Figure 3.2d shows TEM image of the original diatom and Figures 3.2e and 3.2f show the TEM image of the diatom FeOx composite. It is evident that the original diatom was reduced to a nano composite.

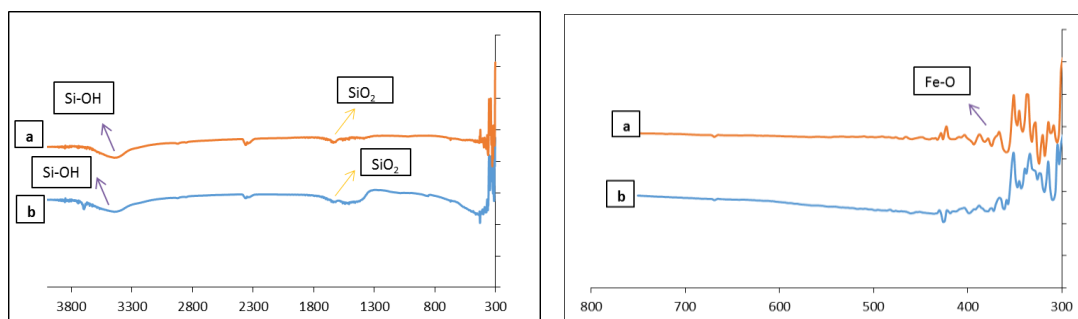


Figure 3.3 FTIR spectra of Diatom (a), diatom – Fe oxide composite. Left is between 300-4000 cm^{-1} and right is the expanded view from 300 to 800 cm^{-1} .

The FTIR spectrum (Figure 3.3) was used to confirm the functional groups. The observed peak at 422 cm^{-1} was attributed to Fe-O vibration [27] while the peaks at 1624 and those between 3300 cm^{-1} to 3500 cm^{-1} were due to vibrations of SiO₂ network and free silanol groups (Si-OH) [86, 87]. TGA was used to test the thermal stability of the diatom-FeO_x (Fig. 4). The weight loss below 120°C was attributed to the removal of physisorbed water while the loss between 120-300 °C was due to chemisorbed water [88]. In the 300-400 °C range, the weight loss was from the oxidation and decomposition of mercaptopropyl or aminopropyl groups on the diatom surface. The exothermic weight loss in the range of 400-600°C was due to the decomposition of strongly tethered organosilanes and dehydration of silanol groups, and the weight reduction between 400–800 °C was due to the dehydroxylation of the silica surface [89, 90].

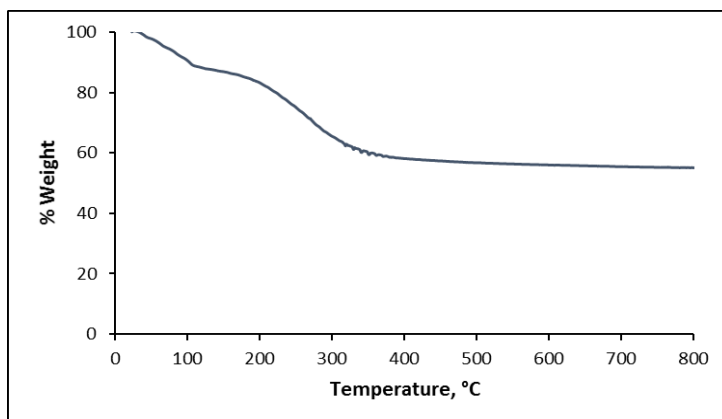


Figure 3.4 TGA of diatom-Fe oxide composite.

The TGA (Figure 3.4) indicated that diatom-FeOx exhibited good thermal stability. It is worth noting that the observed weight loss (35%) below 300 °C was mainly ascribed to the evaporation of water and the mass remained as residue beyond 800 °C. The residue was 45%.

3.3.2 Adsorption Kinetics

Arsenic was not adsorbed on the pure diatom, but diatom-FeOx was effective in removing arsenic from water. 0.014 g of adsorbent was contacted with 100 ml arsenic containing water. Arsenite concentrations of 61, 89, 133, 193, 299 ppb and arsenate concentrations of 64, 103, 150, 213, 334 ppb were studied. Adsorption increased with contact time. Percent adsorption was calculated as described in Section 2.3.2.

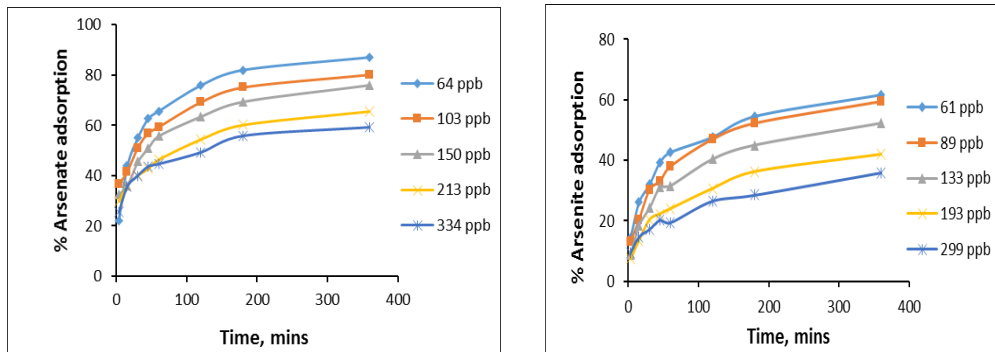


Figure 3.5 Percent adsorption of arsenite (a) and arsenate (b) as a function of time, adsorbent dosage 0.014 g in 50 mL of solution.

Figure 3.5 shows percent adsorption as a function of time. Highest adsorption was seen in the first 45 min of exposure. The slower adsorption was due to the decrease in concentration gradient between the bulk solution and the sorbent surface, which decelerated the transport of the arsenic species to the diatom-FeOx. Similar trend has been reported before for the adsorption of arsenic on granular ferric hydroxide [91] and ferrihydrite [92].

The amount of arsenic adsorbed, adsorption capacity q_e was calculated using as describes in section 2.3.2.

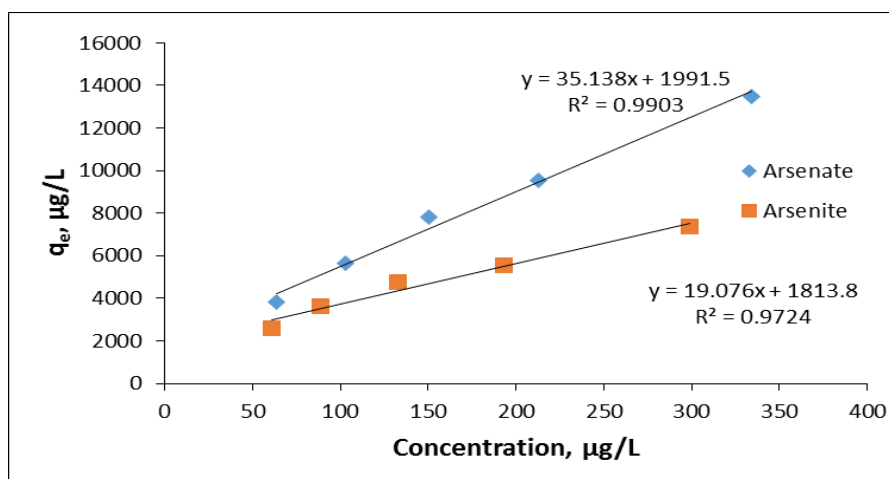


Figure 3.6 Adsorption capacity of arsenite and arsenate at equilibrium.

Figure 3.6 presents the q_e at different arsenic concentration. Initial concentration is known to influence the adsorption capacity, this is in line with previously reported data [93]. It was seen that arsenic adsorbed at any residence time was higher for a higher initial arsenic concentration. As expected, q_e also increased with initial arsenic concentration due to the greater driving force [94].

Table 3.1 First Order and Second Order Kinetics of Arsenite and Arsenate

Concentration	First Oder			Second order		
	q_e ($\mu\text{g/g}$)	K_1	R^2	q_e ($\mu\text{g/g}$)	K_2	R^2
Arsenite						
61	2861	$1.98 \cdot 10^{-2}$	0.92	2694	$1.37 \cdot 10^{-5}$	0.99
89	4658	$2.10 \cdot 10^{-2}$	0.92	3875	$7.79 \cdot 10^{-6}$	0.99
133	6570	$2.16 \cdot 10^{-2}$	0.90	5084	$5.57 \cdot 10^{-6}$	0.99
193	8299	$2.21 \cdot 10^{-2}$	0.90	5971	$4.21 \cdot 10^{-6}$	0.99
299	1100	$2.23 \cdot 10^{-2}$	0.86	7699	$3.62 \cdot 10^{-6}$	0.98
Arsenate						
68	3395	$2.08 \cdot 10^{-2}$	0.95	3961	$1.39 \cdot 10^{-5}$	0.99
103	5064	$2.15 \cdot 10^{-2}$	0.94	5846	$9.93 \cdot 10^{-6}$	0.99
151	8170	$2.23 \cdot 10^{-2}$	0.91	8112	$6.14 \cdot 10^{-6}$	0.99
213	10047	$2.27 \cdot 10^{-2}$	0.91	9900	$5.12 \cdot 10^{-6}$	0.99
334	12795	$2.35 \cdot 10^{-2}$	0.92	13875	$4.63 \cdot 10^{-6}$	0.99

First and Second order kinetics were modelled as described in Section 2.3.2. Table 3.1 presents the first and second order kinetics data where the best fit was obtained based on the linear regression coefficient R^2 . The models were fitted with the experimental data at different initial arsenic concentration. Ho and Mac Kay second order equation was found to be a better fit (R^2 is 0.999) as compared to the first order equation. For first order, a larger adsorption rate constant usually

represents quicker adsorption whereas for second order, a lower value of k represents faster adsorption. Based on percent adsorption and kinetics, diatom-FeOx showed higher arsenate adsorption capacity and rate compared with arsenite. The higher removal rate of arsenate relative to arsenite may be due to the rate limiting oxidation of arsenite to arsenate preceding the adsorption [73].

When iron oxides are exposed to water, metal ions on the oxide surface coordinate with OH groups, which either bound to or released H^+ ions depending on the pH and surface charge. The adsorption properties of these oxides are due to the existence of these OH_2^+ , OH and O^- functional groups. Arsenic may be removed by ligand exchange with OH and OH_2^+ functional groups on the surface forming an inner sphere complex. An incompletely dissociated acid $H_2AsO_4^-$ provides a proton for complexation with OH group to form H_2O and provide space for anion adsorption. The arsenic species may also be removed through complexation with oxyhydroxide sites on the adsorbent surface according to:

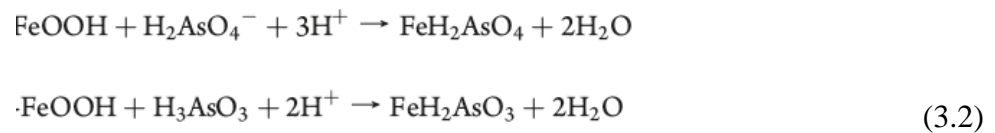


Table 3.2 Langmuir, Freundlich and D-R Model Parameters for Diatom-Fe Oxide Composite

	Langmuir model		Freundlich model		D-R model	
	q_m ($\mu\text{g/g}$)	K_L	n	K_f	q_m (mol/g)	E (kJ/mol)
As(III)	10,000	0.015	0.47	708	0.0017	12.9
As(V)	12,500	0.050	0.45	1491	0.0020	12.9

Langmuir and Freundlich adsorption isotherms provided an insight into the surface coverage via physisorption or chemisorption and were calculated as describes in Section 2.3.2. The Langmuir maximum adsorption capacity of arsenite on the composite was 10,000 $\mu\text{g/g}$ and arsenate was 12,500 $\mu\text{g/g}$. The Langmuir constant b , the ratio of adsorption n to desorption rate constant is an indication of affinity of the sorbent material towards arsenic. The correlation coefficients R^2 for the Langmuir model were 0.99. Since R_L was less than 1, the adsorption was considered favorable. Hence Langmuir model effectively explained the arsenite and arsenate uptake by diatom FeOx composite.

A measure of adsorption capacity and intensity was provided by the Freundlich constants k_f ($\mu\text{g/g}$) and $1/n$, respectively. Here, n was an indicator of the degree of nonlinearity between water concentration and sorption ($n=1$ denotes linear adsorption, $n < 1$ a chemisorption and if $n > 1$ implies physisorption. The bond energy increases proportionally with surface density for $n < 1$ and vice versa for $n > 1$. A value of n less than 1 implied that the adsorption was a chemical process, and that the bond energy increased with surface coverage.

The D-R model was also used to obtain the adsorption capacity q_m (mol/g.) and the mean free energy of sorption [$E = (-2\beta)^{-1/2}$] to yield information about the

sorption being physical or chemical interactions. The experimental data was also modelled with D-R isotherm as:

$$\ln q_e = \ln q_m - \beta \varepsilon^2 \quad (3.3)$$

where q_e (mol/g) is equilibrium adsorption, q_m is adsorption capacity, β is activity coefficient related to the mean free energy of sorption, and $\varepsilon = RT \ln(1 + 1/C_e)$ is Polanyi potential, $R = 8.314 \text{ J k}^{-1} \text{ mol}^{-1}$, $T = 293 \text{ K}$, and C_e is equilibrium concentration (mol/L). The data showed good fit with high R^2 value. The q_m for arsenite was 0.0017 mol/g and for arsenate was 0.002 mol/g . The values of E provided information about sorption type, i.e. physical or chemical. An E between 8 and 16 KJ/mol is attributed to a chemical process while an $E < 8$ is considered physical. The energy for both arsenite and arsenate was between 8 and 16 kJ/mol, thus process the process was considered chemisorptions. The monolayer Langmiur adsorption capacity for diatom-FeOx composite was excellent and higher than those listed for carbon nanotube, sand and limestone supports and as well as granular ferric hydroxide

3.4 Conclusion

This chapter highlights the potential application of diatom frustules as the host for immobilizing nanomaterials to form a composite for water treatment. Iron oxide was successfully immobilized on the diatom by precipitation on live algae cells and the organic algal mass was removed via H_2O_2 treatment. The FeOx on the diatom surface was effective in removing both arsenite and arsenate with somewhat higher percent removal for arsenate. It took 45 minutes to reach equilibrium adsorption, and the Langmuir adsorption capacity for arsenite and arsenate were 10,000 and 12,500 $\mu\text{g/l}$, respectively. The DR-model suggested that the adsorption was via a chemical process.

CHAPTER 4

SYNTHESIS OF BIMETALLIC OXIDE ON DIATOM FOR THE REMOVAL OF SELINIUM FROM WATER

Selenium is an important micronutrient for animals and humans but is toxic in excess [95]. Higher Se concentration can lower reproduction rates and increase birth defects [96, 97]. In water, Selenium exists predominantly in inorganic forms selenite (SeO_3^{2-} , where Se is present as the Se^{4+} and selenate (SeO_4^{2-}) where selenium is present as the Se^{6+} [98]. The toxicity of selenium depends on its oxidation state and Se (IV) is considerably more toxic than Se (VI) [99]. Drinking water is a primary source for selenium exposure and the U.S. Environmental Protection Agency has set the maximum contaminant level in drinking water to be 0.05 mg/L. Sources of Se include agricultural and mine drainage, residues from fossil fuel thermoelectric power plants, oil refineries and metal ores [100].

Variety of treatment technologies have been explored for the remediation of both selenium oxoanions in water. These include bacterial reduction, membrane filtration, chemical reduction, reverse osmosis, and solar ponds [101-103]. These technologies have their limitations and alternative treatment techniques are being explored. Adsorption by metal oxides of iron and aluminum have shown promise in selenium removal [104]. Other materials like Mg/Fe hydrotalcite type compounds, hematite, magnetite, iron-coated GAC and magnetic Fe/Mn oxide nanomaterials also have high affinity for selenium [105-109]. Adsorbents such as sulphuric acid-treated peanut shell, hydrocalumite, ettringite, AlPO_4 , biopolymeric materials, aluminum-based water treatment chemicals, hardened cement paste, cement minerals, aluminium oxides, iron

oxyhydroxides, iron coated sand, and zero valent iron [110-117] have also been tested for Se removal.

Nanostructured adsorbents containing an active sorbent on an inert support have shown excellent potential in water treatment [12]. Typical supports include those based on different carbons, silica, cellulose and polymers [24-26] whereas metal oxides, metal, carbon nanotubes and ion exchange have been used as sorbents [27-29]. There has also been an interest in developing biological materials as supports for sorbents and recently we have reported the use of diatom frustules as supports for iron and zirconium oxides for removing fluoride and arsenic from water. The diatom surface can have different functionalities and this facilitates the immobilization of different materials [10, 11].

It has been reported that mixed metal oxides can exhibit better sorption abilities than individual oxides in terms of higher capacities, pH tolerance and faster kinetics [118, 119]. Among these, hydrous zirconium oxide is known to retain various oxo metal anions, especially those that can form weak conjugate acids [120]. At the same time the iron oxides/hydroxides and have been gaining popularity in water treatment and are known to adsorb Se [119]. The objective of this research was to develop nano sorbents by immobilizing mixed metal oxides iron and zirconium oxides on diatom frustules.

4.1. Synthesis of Bimetallic Diatom Composite

Diatom *Phaeodactylum tricornutum* was cultured in artificial sea water and used to make metal oxide composites using method mentioned before [38]. 6L of diatom

culture was flocculated with 6 g of $ZrOCl_2 \cdot 8H_2O$ and 6 g of $FeCl_3 \cdot 6H_2O$ (both from Sigma Aldrich) at pH 9, which was adjusted using 1 M NaOH. The bimetallic diatom mixture was separated by gravitational settling and membrane filtration. This was then washed with 500 mL Milli-Q water, heated at 70°C in an oven for 6 hr and then treated with 10 ml of conc. H_2SO_4 before heating for 2 hrs at 200°C. The material was vacuum filtered, washed with Milli-Q water to neutral pH and then dried at 200°C in a vacuum oven. The resulting bimetallic oxide-diatom composite (BMDC) was characterized using SEM (LEO 1530 VP), TEM, Thermogravimetric Analyzer (Pyris 1 from PerkinElmer Inc), BET surface area analyzer (Quantachrome Autosorb-1), and FTIR (IR Affinity -1, Shimadzu).

4.2 Adsorption Studies

The kinetics of adsorption was performed as reported before. A 50 millilitre of 5 mg/L of Se (IV) and (VI) solutions were contacted with 0.010 g and 0.025 g of adsorbent and the samples were collected at 5, 15 and 30 minutes as well as 1, 3, 6 and 24 hours. 5 mL aliquot was withdrawn at different time intervals, and the residual Se in the media was quantified using Agilent 7500 ICP-MS. All standards were prepared from multi-element solution 2A, 10mg/L (Spex Certiprep) with the addition of internal standard mix [59]. The adsorption isotherms and capacity (q_e) were obtained by varying the mass of adsorbent from 0.002 to 0.015 g (Se IV) and 0.002 to 0.050 g Se (VI) at pH 6. The samples were collected for analysis after 0, 6 and 24 hours of adsorption. Adsorption was studied at pH 2, 4, 6 and 8 by contacting 0.010 g of adsorbent for 24 h with 50 millilitres of 1 mg/L Se(IV)

solution. Desorption of selenium from the used BMDC was carried as follows. After selenium adsorption, the composite was washed with 1M NaCl, followed by distilled water and 0.1 M NaOH.

4.3 Results

4.3.1 Characterization of Bimetallic Oxide-Diatom Composite

Diatom was grown till the late exponential phase which after the addition $ZrOCl_2 \cdot 8H_2O$, $FeCl_3 \cdot 8H_2O$ and NaOH led to the precipitation of Zr and Fe oxides. The H_2SO_4 treatment decomposed the organic mass leaving the frustule core coated with Zr and Fe oxides. The presence of Zr and Fe particles on diatom surface was studied using SEM.

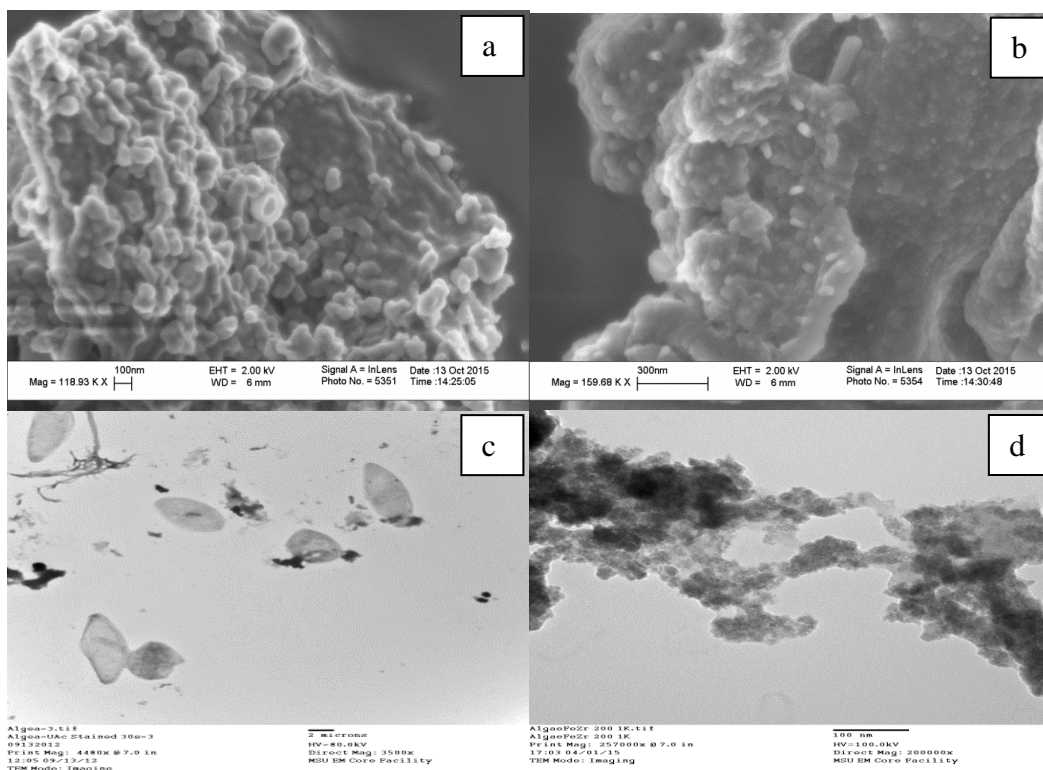


Figure 4.1 (a) SEM of diatom, (b) diatom bimetallic oxide composite; (c, d) represents mapping for Zr and Fe immobilized on diatom surface. TEM of (e) diatom and (f) diatom bimetallic oxide composite

Figure 4.1a shows SEM of the original diatom, Figure 4.1b is bimetallic composite and Figures 4.1c and 4.1d are mapping of Zr and Fe from BMDC. Similarly, Figures 4.1e and 4.1f show TEM image of the diatom and BMDC. SEM and TEM images showed that the original diatom was reduced to porous nano biosilica. EDX analysis using SEM confirmed the presence of Zr (89.87%), Fe (8.75%) in BMDC. The specific surface area of bimetallic diatom composite based on BET measurements was found to be $128 \text{ m}^2/\text{g}$ and pore diameter was 9.39 \AA .

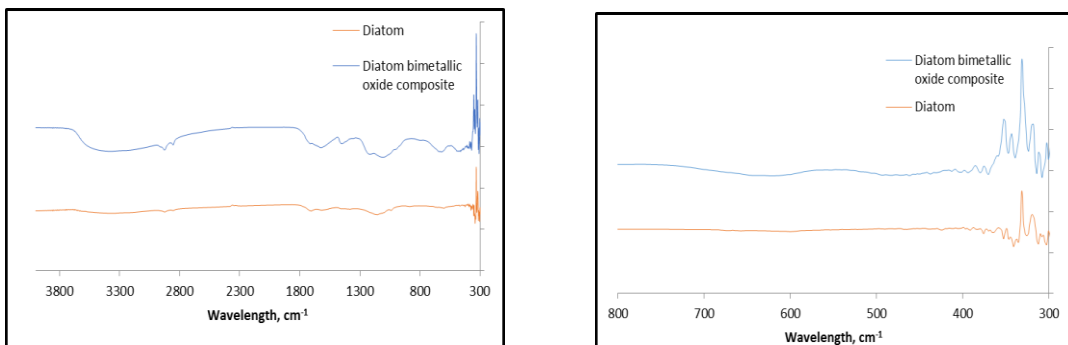


Figure 4.2 FTIR spectra of Diatom and Diatom bimetallic oxide composite (left), enlarged view of the spectra (right)

The FTIR (Figure 4.2) was used to confirm the functional groups. The observed peak at 374-400 cm^{-1} was attributed to Zr-O vibration, which confirmed the ZrO_2 structure [53]. The observed peak at 551 cm^{-1} and around 700 cm^{-1} was attributed to Fe [121]. Both spectra showed peaks at 1108 and between 3300 cm^{-1} to 3500 cm^{-1} . These were due to stretching of siloxane (Si-O-Si) and free silanol group (Si-OH) [55].

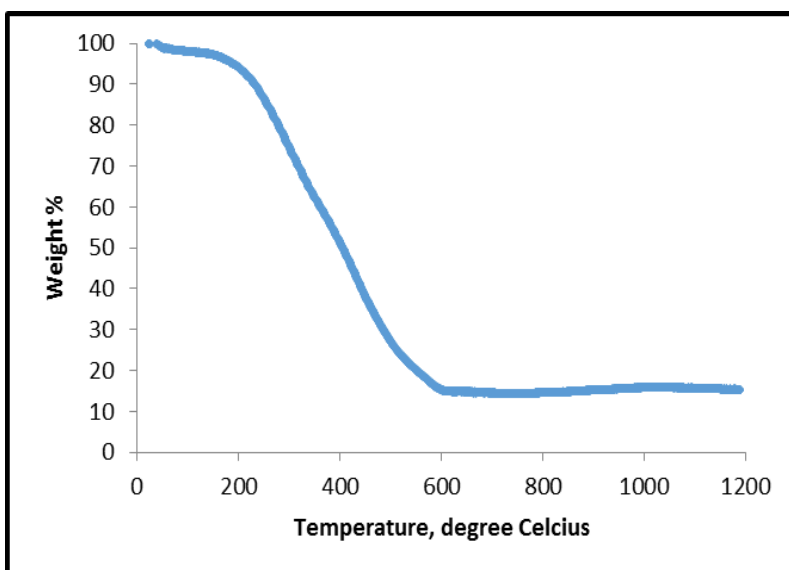


Figure 4.3 TGA of Bimetallic oxide diatom composite.

TGA was used to test the thermal stability of the BMDC (Figure 4.3). Physisorbed water was lost below 120 °C while chemisorbed water removed between 120-300 °C [56]. In weight loss in the 300-400°C range was from the decomposition of mercaptopropyl or aminopropyl groups on diatom surface. The temperature range between 400-600 °C saw the loss of strongly tethered organosilanes and dehydration of silanol groups, and the weight loss in the 400–800 °C was due to the dehydroxylation of the silica surface. [57, 58].

4.3.2 Selenium Removal using Bimetallic Oxide Diatom Composite

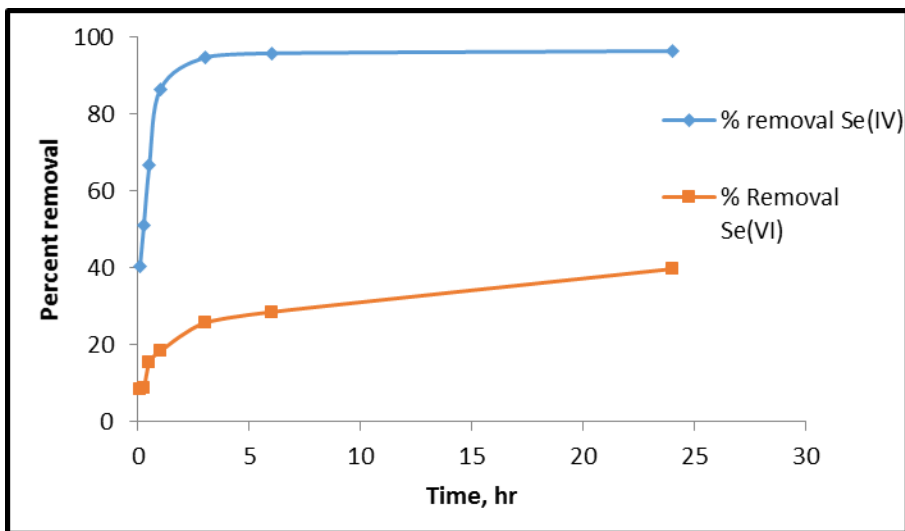


Figure 4.4 Percent removal of Se (IV) and Se (VI) as a function of time.

It was observed that no selenium was adsorbed on the pure diatom, but the BMDC was effective in removing selenium from water. Selenite and Selenate uptake by BMDC was studied as a function of time and is presented in figure 4.4. Selenium sorption increased as a function of contact time. Selenium sorption increased as a function of contact time. 0.010 g of bimetallic composite showed Se (IV) uptake of

50 and 95% at 15 mins and 3 hrs, respectively, whereas 0.025 g of bimetallic composite showed removal only 40% Se (VI) after 24hrs of contact. This shows that bimetallic diatom composite shows better Se (IV) removal efficiency compared with Se (VI).

Table 4.1 Experimental q_e , using Different Concentration of Adsorbent Doses

Initial Adsorbent Concentration (g)	Experimental q_e mg/g	% Removal
Se(IV)		
0.001	56.24	56.24
0.002	45.41	90.82
0.005	19.12	95.64
0.010	9.67	96.74
0.015	6.45	96.80
Se(VI)		
0.002	10.61	21.23
0.005	5.51	27.55
0.010	3.26	32.60
0.015	2.43	36.49
0.050	0.89	44.90

At equilibrium, the percentage removal increased with the adsorbent concentration while q_e decreased. These are presented in Table 4.1. It was seen that the initial adsorbent dose affected q_e which dropped from 56.24 mg/g for 0.001 g of adsorbent to 6.45 mg/g for 0.015 g for Se(IV). For Se (VI), the capacities were 10.6 mg/g for 0.002 g of adsorbent to 0.89 mg/g for 0.05 g. The kinetics of selenium uptake was studied using conventional Langereen [59] as well as Ho and Mckay kinetic models [60].

Table 4.2 First Order and Second Order Kinetics

	First Order			Second Order		
	q _e	K	R ²	q _e	K	R ²
Se (IV)	1.92	0.0056	0.91	4.75	1.4	0.99
Se (VI)	0.564	0.0013	0.89	0.73	0.54	0.98

The applicability of first and second order models were tested for adsorption of Selenium on BMDC and the data are presented in Table 4.2. The second order equation was found to be a better fit (r^2 0.999). A larger adsorption rate constant in the first order equation usually represents faster adsorption whereas a lower value of k represents faster adsorption in the second order.

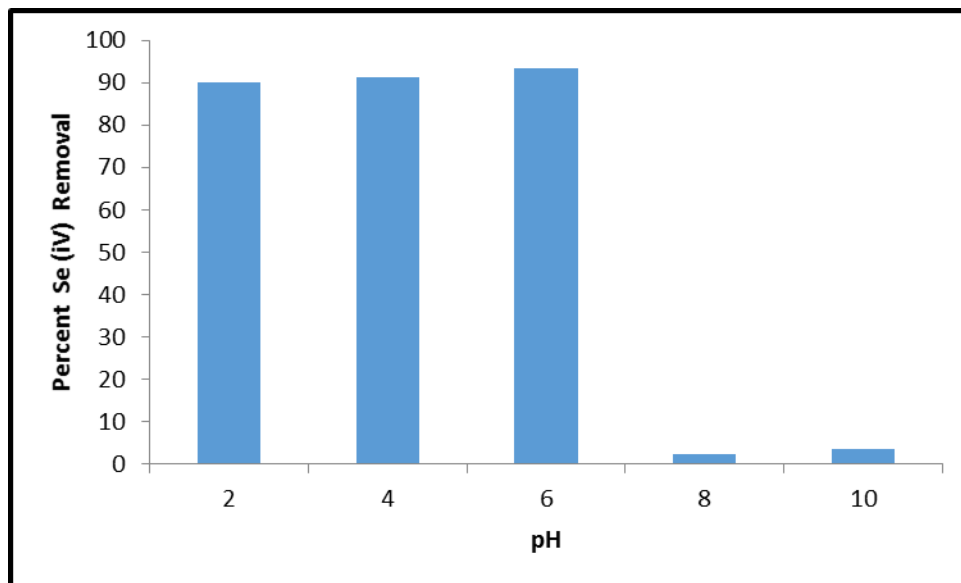


Figure 4.5 Effect of pH on Se (IV) removal.

The effect of pH was studied at 2, 4, 6, 8 and 10 (Figure 4.5). The variation in pH in the range of 2 to 6 didn't show much effect on percent adsorption. With increase in pH from 6 to 10, the adsorption capacity decreased. At low pH conditions, the H_3O^+ ion concentration was optimum to make the surface of the BMDC positively charged and hence accessible for selenium ions. With an increase in pH, especially in alkaline medium, the selenium uptake was reduced due to the competition with OH^- , which also had high affinity for the zirconium and iron ion.

Langmuir [65] and Freundlich [66] isotherms were used to study surface coverage via physisorption and/or chemisorption and were calculated as described in Section 2.3.2.

Table 4.3 Model Parameters of Langmuir and Freundlich Isotherms for Adsorption of Selenium

	Langmuir model			Freundlich model		
	q_m (mg/g)	b	R^2	n	K_f	R^2
Se (IV)	277	0.205	0.95	1.21	0.0103	0.95
Se (VI)	0.48	0.252	0.95	6.07	0.0021	0.95

The Langmuir parameters are presented in Table 4.3. The maximum adsorption capacity for Se (IV) on the composite was 277 mg/g and Se(VI) was 0.48 mg/g at pH 6. The Langmuir constant b, the ratio of adsorption and desorption rate constants are indications of affinity of the BMDC and selenium. Since R_L was less than 1, the adsorption was considered favourable. Hence,

Langmuir model effectively explained the selenium uptake by the BMDC. The values for k_f (mg g^{-1}) and n are presented in Table 3. [69]. The values of n (0.47 and 0.45) indicated that the adsorption was a chemical process, and that the bond energy increased with surface coverage [66]. The correlation coefficient, R^2 , was 0.95.

Adsorption of Se on metal oxides can occur due to both outer and inner sphere complexation [76]. Based on the second order kinetics, Langmuir and Freundlich models, the adsorption of Se on BMDC appeared to be via a chemical process. Selenate is known to be more strongly adsorbed than selenite at a wide range of pH. As per the recent review, mixed metal oxide, double layered materials and adsorbents based on natural materials have shown good sorption capacities and relative fast kinetics. It is worth mentioning that the sorption capacity from our study is comparable to those reported before. For example a q_m of 2.38 mg/g was reported for selenate removal using Fe_3O_4 [63], 26.3 mg/g using FeOOH [64, 122], 29.0 mg/g using Fe-Mn hydrous oxide [12] and 74.9 mg/g Se (IV) using Green algae *Cladophora hutchinsiae* [123].

Desorption of Se (IV) and regeneration of BMDC was studied by monitoring the effluent washes from a Se (IV) sorbed BMDC. 0.050 g of adsorbent was contacted with 50 mL of 2 mg/L of Se (IV) solution. After 24 hours of exposure, the solution was vacuum filtered using 0.2 μm filter and washed with 1 M NaCl followed by distilled water and 0.1 M NaOH solutions. NaCl wash desorbed only a small amount of Se (IV) indicating that only a small fraction of these ions are held by ion-exchange or electrostatic type forces. Nearcomplete desorption of Se (IV) was achieved by NaOH wash removed the sorbed Se (IV) by

competing for the active sites. In short, the Se (IV) could be regenerated relatively easily by treating with an alkaline solution (e.g., 0.1 M NaOH). Sodium hydroxide desorption did not damage the BMDC which could be reused after regeneration with 0.1 M H₂SO₄ acid, and two successive regenerations showed more than 90% removal efficiency.

4.4 Conclusion

A bimetallic composite was successfully synthesized by immobilizing iron and zirconium on diatoms. This was effective in removing Se from water. Maximum Se (IV) adsorption capacity of 277 mg/g adsorbent was calculated using the Langmuir adsorption isotherm. The adsorption capacity was unchanged between pH between 2 and 6, but decreased rapidly at pH 8. The BMDC had a higher adsorption capacity for Se(IV) when compared with Se(VI).

CHAPTER 5

ANTISOLVENT PRECIPITATIVE IMMOBILIZATION OF A NANOSTRUCTURED HYDROPHOBIC DRUG ON SILICA FROM LABORATORY CULTURED DIATOM

A large percentage of all drug molecules developed in pharmaceutical industry are hydrophobic and consequently have low aqueous solubility as well as bioavailability [43]. Dissolution is a limiting factor in their *in vivo* performance and increasing this is a major challenge [44]. Surface area enhancement via nanostructuring has been a common approach to increasing the dissolution rate [45]. Nano drug particles have been synthesized via top-down approaches such as milling or high pressure homogenization as well as by crystallization techniques [46]. Other approaches to enhance dissolution includes complexation with cyclodextrin [47], microemulsion formation [48], encapsulation in polymer films [49] and deformable membrane vesicles[50].

Silica based materials with different porosity have been extensively used in industry for drug delivery and controlled release. They are biocompatible, have high surface area, thermal stability and their porous structure can provide a means for diffusion controlled release [124, 125]. Mesoporous silica nanoparticles have been most popular due to their porosity, inertness and their surface functionality have been manipulated to alter chemical properties. Nanosilica have also been used for the delivery of hydrophobic drugs via surface loading, making dispersion or by adding surfactants or wetting agents. Not only have they been used to increase drug solubility and controlled release, they have been used as imaging agents [126]. Porous silica has been synthesized by different methods such as sol-gel chemistry, evaporation, spray drying, and reaction of

templated tetraethyl orthosilicate [126]. Typically, these synthesis processes are expensive, time consuming and require the use of toxic chemicals. Diatomaceous earth which is often contains impurities such as minerals from rocks and clay have also been used for drug delivery and as magnetically-guided micro carriers [127]. Considering everything, a biosilica that can be cultured in a laboratory can be an useful material for drug delivery.

Diatom nanotechnology, where nano scale silica from unicellular microalgae is used in real-world applications is evolving to be an important research area. The diatoms are found in fresh as well as seawater, have unique porous structure and have excellent mechanical properties and chemical inertness [2, 3]. They have been used in various applications including optics, photonics, bio sensing, filtration, immune precipitation, micro and nanofabrication, protein separation, water treatment and catalysis [128-131]. They are excellent candidates for drug delivery, an application that is yet to fully exploited. To the best of our knowledge, there is only one publication so far where frustules isolated from laboratory cultured diatoms has been used as carriers for the hydrophilic drug streptomycin [132]. The wide range of microalgae represent diverse frustule morphology that could potentially be used to vary drug release characteristics [1]. The objective of this study was to use diatom frustules for delivery of hydrophobic drugs by antisolvent precipitation of the drug molecule on the frustules to develop drug nanostructure for enhanced release. Another specific objective is to study Griseofulvin, an antifungal BCS class II drug that is only slightly water soluble (8.64 mg/L) [133].

5.1 Preparation of Diatom-Drug Composite

Griseofulvin (95% pure), hydroxypropyl methyl cellulose form (HPMC, mol. wt. 10,000, viscosity of 5 cP, 2 wt.% in H₂O) were purchased from Sigma Aldrich, and diatom *Phaeodactylum* was purchased from marine bioglow. The diatom was cultured and maintained in Aquil using a method described before [38]. Artificial sea water was maintained in diurnal Chamber with 12 hour day/night cycles at 19°C±1°C. Exponential phase diatom culture was flocculated with one molar NaOH. The culture was separated by gravitational settling and membrane filtration and washed with Milli-Q water. The organic matter was decomposed by treating with concentrated H₂SO₄ followed by heating at 200°C for 2 hrs [25]. This was followed by vacuum filtration, wash with Milli-Q water to neutral pH and then drying at 200°C in a vacuum oven. The acid treatment also functionalized the diatom silica.

Griseofulvin was loaded on the diatom silica via antisolvent precipitation at room temperature. This was carried out as follows. It was dissolved in methanol to form a clear solution. Diatom silica was wetted with MQ water, HPMC was added and sonicated for 1 hour. The drug solution was added to the aqueous phase slowly while undergoing sonication. After complete addition, the suspension was sonicated for 1 hr and dried at 100°C. The ratio of Drug, diatom, HPMC were 3:3:1. The final solid containing the diatom nano silica and the drug was referred to as the drug-diatom composite or DDC.

5.2 Characterization of Drug-Diatom Composite

Scanning electron microscope (SEM; LEO 1530VP) was used for studying the morphology of drug and DDC, respectively. A Nicolet Almega XR Dispersive Raman with Olympus BX51 Confocal Microscope (Thermo Electron Corp.) using a 532nm laser was used for Raman imaging. The samples were placed on glass slides for the detection using 100 × optical lenses. For FTIR (IR Affinity -1, Shimadzu) analysis, the sample was pressed with KBr to form a pellet. Particle size analysis was carried out by using Beckman Coulter, N4 Plus Submicron Particle Size Analyzer at 23° fixed detector angle. Zeta potential measurements were determined using a DelsaNano (Beckmann Coulter). This was determined from the electrophoretic mobilities using the Smoluchowski equation. All measurements were performed at 25 °C. Dissolution tests were carried out using USP II paddle apparatus and Griseofulvin content was measured by UV spectrophotometer.

5.3 Dissolution test

Dissolution was carried out with a Distek Dissolution tester (North Brunswick, NJ) according to the USP II paddle method. De-ionized water (1000 ml) was used as the dissolution medium and was maintained at 37° C. A paddle speed of 50 rpm was used. The DDC was weighed equivalent to a Griseofulvin dose of 8.9 mg and added to the dissolution medium. Aliquots of 4 ml were taken manually at intervals of 2,5,10, 20 30, 60, 120, 180 and 240 mins, filtered using 0.2 um filter and analyzed for Griseofulvin content using UV spectrophotometer at 295 nm. The physical mixture of drug and HPMC was also used in the dissolution test. To determine amount of drug in the diatom

composite, the 2 mL of methanol was added to the DDC and sonicated for 30 mins. The solution was filtered, diluted with DI water and measured for drug content using a UV spectrophotometer. All the experiments were carried out in triplicates.

5.4 Results

Diatom culture was grown for 10 days. The cells were collected and the organic matter was successfully removed via acid and heat treatment as described before [134]. The diatom silica thus obtained was utilized to prepare DDC. The details of the diatom frustules have been presented in Chapter 2.

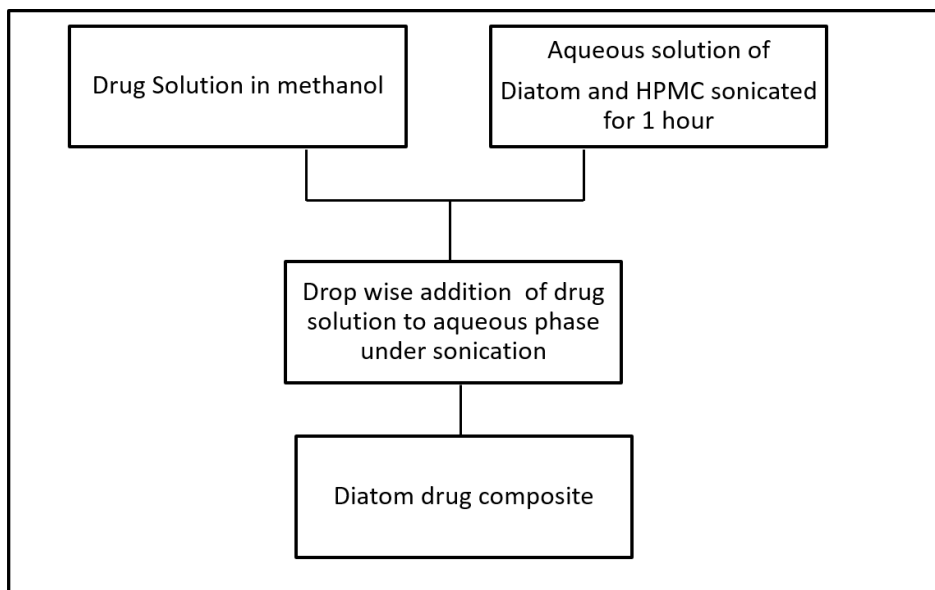


Figure 5.1 Preparation of diatom drug composite.

Figure 5.1 shows the preparation process. Antisolvent precipitation was used to generate Griseofulvin crystals that were deposited on the diatom surface. The presence of HPMC helped inhibit growth of crystals size and was in line with what has been reported before [135]. Ratio of Diatom:Griseofulvin:HPMC was 3:3:1. Sonication was used to

facilitate rapid and uniform nucleation that helped the formation of small and uniform size particles. Figure 5.2a shows the pictures of vials containing the drug, and DDC.

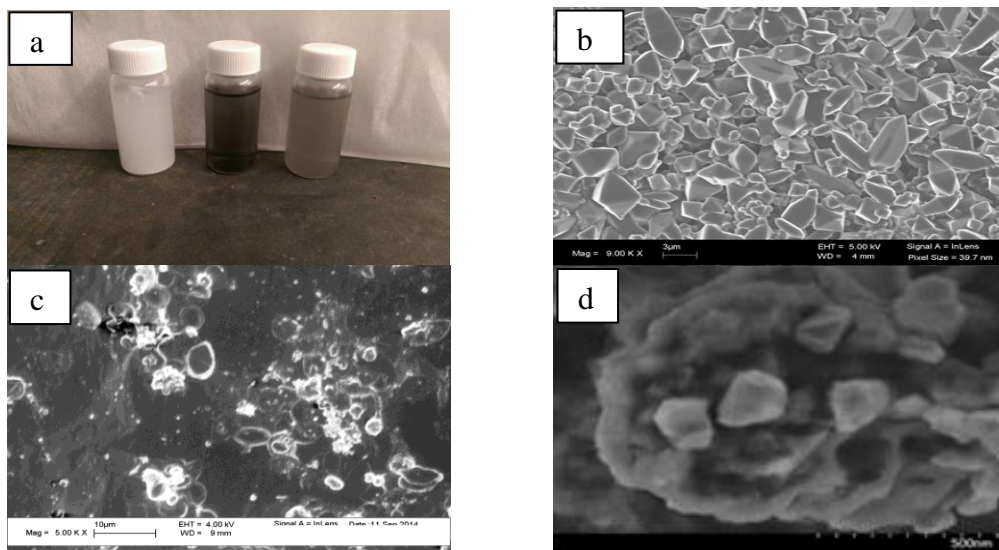


Figure 5.2 (a) Photograph of vials containing pure drug, diatom and DDC in water (left to right), (b) SEM of pure drug and (c) diatom (d) diatom-drug composite.

SEM of Griseofulvin and DDC are shown in Figure 5.2. It is evident that griseofulvin crystals were formed on the diatom surface. Particle size measurements using static light scattering at 23 degree scatter angle showed a mean particle size of 1034 nm for diatom and 3000 nm for DDC. The increase in particle size was attributed to the drug loading. Zeta potential measurement using was -13 mV in aqueous solution showing that the DDC particles were less stable.

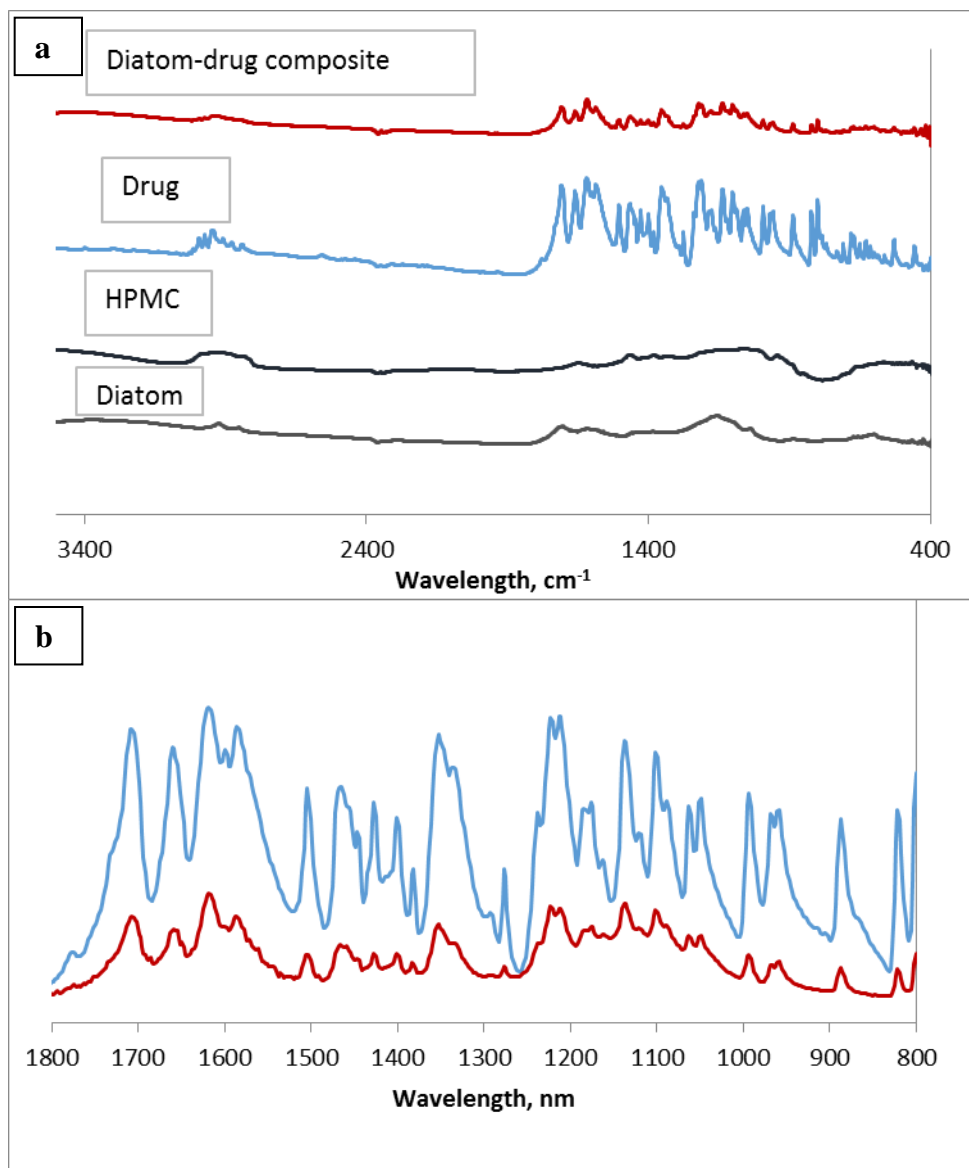


Figure 5.3 (a) FTIR spectra of DDC, drug, HPMC and Diatom, (b) expanded view of DDC and drug.

Figure 5.3 shows FTIR spectra of Diatom, Griseofulvin, HPMC and DDC. The two bands at 3740cm^{-1} and 1630cm^{-1} in the diatom spectra were attributed to the isolated silanol ($\text{m}(\text{O}-\text{H})$) and bending mode of physisorbed water, respectively [136]. Pure Griseofulvin displayed two distinct peaks at 1704 and 1658cm^{-1} which was attributed to the stretching of carbonyl group of benzofuran and cyclohexanone, respectively present in its structure [137]. The peak at 1658cm^{-1} and 1704cm^{-1} were

broadened in the composite spectra. The broadening of these two peaks can be attributed to the hydrogen bonding between isolated silanols located on the surface of diatom and carbonyl group of benzofuran and cyclohexenone of Griseofulvin. Moreover, peaks from Griseofulvin in the range of $1617\text{--}890\text{ cm}^{-1}$ could also be seen in DDC indicating the presence of Griseofulvin.

Raman spectroscopy was used to image the DDC (Figure 5.4). It provided sensitive Griseofulvin detection in DDC and the well-resolved fundamental intra- and/or inter-molecular stretching and bending modes allowing determination in solid state. Figure 4 shows the Raman spectra of diatom, Griseofulvin and DDC. Griseofulvin spectra showed strong peaks in the region $1550\text{--}1800\text{cm}^{-1}$ and $2800\text{--}3200\text{cm}^{-1}$, which were attributed to the C-O stretching of benzofuran ring and C-H stretching of GF, respectively [138]. The same characteristic peaks were also observed in DDC, which indicated the presence of the drug and no significant alteration of the Griseofulvin molecule.

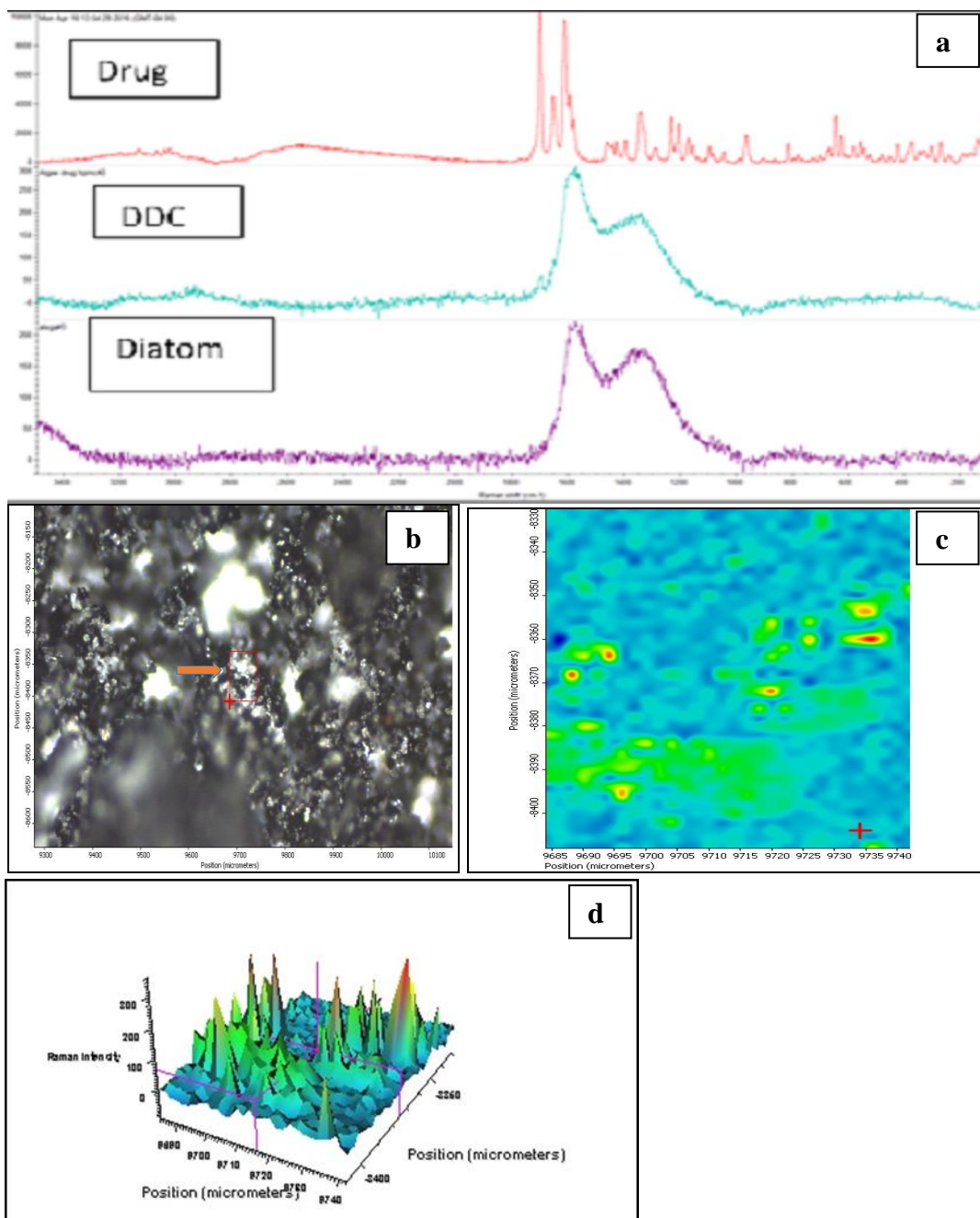


Figure 5.4 (a) Raman spectra and mapping of the diatom drug composite (b) image of the scanned area, (c) drug distribution in scanned area (2D, blue area corresponds to a non-GF background, green and red area to a high GF concentration) (d) 3D chemical Imaging of the scanned area. Scanning was done at 1699cm^{-1} .

Raman chemical mapping was used to image and map the top surface of drug particle. Two particles embedded in the DDC were mapped and figure 5.4c shows the

distribution of Griseofulvin. This was done by plotting the peak area of the selected Raman bands over the entire scanned area. A red color corresponded to a high GF concentration followed by yellow and green, whereas the blue color represents the background. The distribution of drug was seen throughout the scanned area. These observations agreed with the SEM measurements suggesting that drug existed in the form of microparticles dispersed in the diatom.

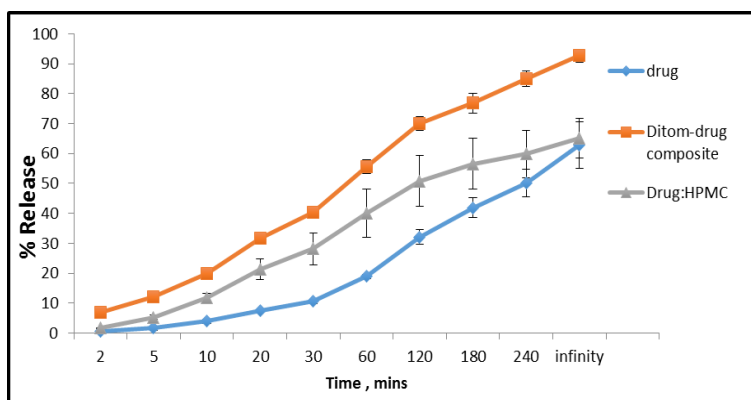


Figure 5.5 Dissolution of pure drug, Drug-HPMC mixture and DDC.

DDC contained 41% of Griseofulvin by weight. The drug release profiles for pure drug, drug-HPMC and DCC are shown in figure 5.1. It is evident that DDC showed increased Griseofulvin release. Pure drug showed release of 20% after 1 hr and 63% after 4 hours. The physical mixture of drug and HPMC showed 40% release after 1 hr and 65% after 4 hours while DDC showed 54% release after 1 hr and 93% after 4 hours. The increased in dissolution following the antisolvent precipitation in presence of diatom demonstrates that the nanoporous silica from the frustule is a good candidate to serve as a carrier for hydrophobic drugs.

5.5 Conclusion

This chapter presents an effective approach for immobilizing hydrophobic drug molecules on a bio nanosilica for enhanced dissolution. Griseofulvin crystals were successfully immobilized on diatom surface via antisolvent precipitation. Diatom-drug composite shows increased dissolution compared with the pure drug. Dissolution enhancement was as high as 33%. Diatom offers unique architecture with excellent surface and mechanical properties with excellent potential in drug delivery area.

CHAPTER 6

EFFECT ON GROWTH, PHOTOSYNTHESIS AND OXIDATIVE STRESS ON SINGLE WALLED CARBON NANOTUBES EXPOSURE TO MARINE ALGAE *DUNALIELLA TERTIOLECTA*

Algae present on surface waters are the dominant primary producers in marine ecosystems [40]. They form a base for the oceanic food web and serve as major components of the global carbon and biogeochemical cycles. Algal populations are affected by anthropogenic pollutants flowing into ecosystems and are important indicators for environment pollution. Nanoparticles with their high surface area and abundant reactive sites can be significant sources of environmental pollution [41]. Algae whose cell walls act as primary sites for interaction with nanoparticles have been effectively used as model organisms to assess nanoparticle ecotoxicity [42].

Due to the extraordinary physical, chemical and electronic properties, the commercial production and use of carbon nanotubes (CNTs) have increased rapidly [42, 139]. Like all other pollutants, the CNTs are expected to end up in soil, water or air [140]. This increases the chance of release into the environment during use and disposal of the products leading to human and ecological risk [141]. CNTs represent a wide range of tubes with different dimensions as well as functionality. Toxicity of multiwalled carbon nanotubes (MWCNT), single walled nanotubes (SWCNT), and double walled nanotubes (DWCNT) have been reported [142, 143]. Influence of MWCNT to fresh water green algae *Chlorella pyrenodisa* [42], *Chlorella vulgaris* [42] and *Chlorella* sp [144, 145] have been studied. Impact of SWCNT on *Raphidocelis subcapitata*, *Chlorella vulgaris* [146] *Pseudokirchneriella subcapitata* [147], *Chromochloris zofingiensis* [148]

and *Scenedesmus obliquus* algae [149] have been reported. Toxicity of CNTs to algae have been mainly attributed to agglomeration and physical interaction with cells, attenuation of photosynthesis and CNT induced generation of intracellular reactive oxygen species [42]. However, given the range of CNT based nanoparticles that can make their way to the environment, there is limited knowledge related to the diversity of possible effects on algal functions.

The SWCNTs and MWCNTs have different geometric structures and hence exhibit different cytotoxicity and bioactivity [150]. While there has been several studies with MWCNTs [42, 145, 151], studies on SWCNTs have been limited. Another important consideration is that not many studies have reported the toxicity difference between different types of CNTs using the same marine species and under similar conditions. A recent study with fresh water algae *Scenedesmus Obliquus* showed marked difference in levels of toxicity [149] between single and double walled CNTs, and another study using fresh water algae *Pseudokirchneriella subcapitata* showed different behavior between metallic and semiconducting SWCNTs [152]. Effects of SWCNT on marine algae, where high salt concentration leads to aggregation is not well understood, and the effects on SWCNT and MWCNT on same marine algae and under similar conditions is yet to be studied. Therefore, the difference between MWCNT and SWCNT are not clearly understood.

The objective of this research was to study the effect of oxidized SWCNTs on photosynthesis activity, growth and oxidative stress using the marine algae *D. tertiolecta*. Since we have published the effect of MWCNT on the same alga [153], another objective

of this paper is to elucidate the difference between these two types of CNTs as applied to algal ecotoxicity.

6.1 Preparation and Characterization of Carbon Materials.

Pristine SWCNTs were obtained from Cheap Tubes Inc. Pre-weighed amounts of purified SWCNTs were mixed with concentrated 1:1 mixture of H₂SO₄ and HNO₃ solution in a reactor and treated in a Microwave Accelerated Reaction System (CEM Mars) at 120°C for 3 and 10 min, respectively to produce different oxidation levels; these are designated as f-SWCNT-A and f-SWCNT-B, respectively. The product was cooled to room temperature, diluted with DI water, and dialyzed until pH neutral (dialysis bag nominal molecular weight cut off 12,000 -14,000 Dalton). The dialyzed SWCNTs were filtered and dried overnight at 60°C under vacuum and were suspended in Milli-Q water at 0.5 mg/mL. The suspension was stable and homogenous. Carbon black was used for comparison and its suspension (Carbot Regal 600 A69) was prepared by adding a known amount to MQ at a concentration 0.5 mg/mL. This suspension was sonicated for 30 minutes but was not stable. Aliquots of the stock suspension were air dried on silicon wafer and analyzed with a field emission scanning electron microscopy with EDX detector (FESEM-EDX, LEO 1530VP).

6.2 Algal Strain and Culturing

Unicellular green algae *D. tertiolecta* (CCMP 1320) was obtained from Provasoli-Guillard National Center for Marine Algae and Microbiota (NCMA), Bigelow Laboratory for Ocean Science, Maine, U.S.A. *D. tertiolecta* was maintained in synthetic

ocean water media (SOW) Aquil without silicate addition [154]. Polycarbonate bottles (Nalgene, 250 mL, cleaned with detergent and acid) were used for maintenance and culturing. The cultures were incubated in a diurnal growth chamber at $19 \pm 1^\circ\text{C}$ with 12h:12h light:dark cycle and $120 \mu\text{mol photons m}^{-2}\cdot\text{s}^{-1}$ illumination from cool-white fluorescence bulbs.

6.3 Exposure Studies

D. tertiolecta was exposed to different carbon materials - Carbon black (CB), f-SWCNT-A and f-SWCNT-B. Test media was prepared by sonicating the 0.5 mg/mL of stock suspension (f-SWCNT-A, f-SWCNT-B and CB,) prior to addition to the culture media Aquil to get nominal concentrations of 0, 0.1, 1, 2.5, 5, 10 and 20 mg/L. This media was allowed to pre-equilibrate for 24-hr on a horizontal shaker (120 rpm). *D. tertiolecta* of late exponential phase was added at 1:100 v:v ratio of inoculums to media. Polycarbonate bottles (125 mL, Nalgene) and borosilicate culture tubes (5 mL, VWR 47729-570) used in this study was pre-cleaned with detergent and acid. The cultures were put on a horizontal shaker (120 rpm) and incubated in the growth chamber. Cultures were set up with 3 – 4 replicates. Additional tests were done by filtering f- SWCNT-A using a $0.2\mu\text{m}$ PTFE filters to remove the aggregates. The filtrate was then tested for toxicity. Throughout the exposure study, control cultures without the carbon material, and blanks (with carbon materials but without algae inoculation) were used to test for interference and agglomeration.

6.4 Culture Analysis

Since the exposure to the SWCNTs might induce oxidative stress, cause growth inhibition and alter photosynthetic functions, the culture analyses focused on observable endpoints for growth, photosynthesis function and oxidative stress.

Algal growth was evaluated with *in vivo* fluorescence, exponential growth rate and total chlorophyll a. Specifically *in vivo* chlorophyll fluorescence (IVF) was measured on daily basis using Turner Designs Trilogy Fluorometer equipped with an optical block of 485 nm excitation and 685 nm emission with a 50 nm bandwidth. The exponential growth rate was obtained from linear regression of logarithmic transformation of *in vivo* fluorescence (LN (IVF)) over time. In addition, total chlorophyll a (chl a) and cell density were quantified. Total chlorophyll a concentrations were estimated by acetone (90% acetone and 10% water mixture) extraction of pigments collected from 50 mL of the culture on a 25 mm GF/F filter. This was followed by Jeffery and Humphrey's trichromatic quantification using Agilent 8453 spectrophotometer following EPA Method 446.0 [155]. Cell density of *D. tertiolecta* was determined using Coulter Counter equipped with a 70 μm aperture tube (Beckman Coulter, Multisizer 3). The particles in the size window 5.2 - 9.6 μm were predominately *D. tertiolecta* cells, while 1.7 – 5.2 μm were from agglomerated CNTs. Measurements were made at a concentration of 20 mg/L.

Scanning electron microscopy (SEM) and light microscope (with immersion oil) were used to view the surface interaction between cells and the f-SWCNTs. For SEM, the cells exposed to f-SWCNTs were filtered onto 0.2 μm polycarbonate filter, rinsed with

MQ water, transferred onto silicon wafer and air-dried. The samples were carbon coated (Bal-TEC 020 HR Sputtering coater) and viewed under scanning electron microscope.

6.5 Photosynthesis

Algal photochemical function was evaluated using Photosystem II (PSII). The photochemical parameters were recorded on a daily basis during mid- to late exponential growth phase by subjecting aliquots of the cultures to dark-adaption (15-min) followed by fluorescence induction and relaxation characterization using Satlantic FIRE System (Satlantic, Inc) under single turnover flash protocol [156]. The protocol generates PSII maximum quantum yield (F_v/F_m), optical cross section σ ($\text{\AA}^2/\text{quantum}$), connectivity factor (p), and several other parameters on the magnitude and rate of fluorescence relaxation ($\alpha_1, \tau_1, \alpha_2, \tau_2, \alpha_3, \tau_3, \tau_{av1}, \tau_{av2}$).

6.6 Glutathione

Total glutathione was quantified for algal cells to evaluate the oxidative stress that might be induced by the exposure to f-SWCNTs. Total glutathione was determined following procedure reported before (Wei et al. 2003). Known aliquots of the algal cultures were filtered on GF/F filters. The collected algal cells were heated in 10 mM methanesulfonic acid at 70°C for 2 min and then sonicated (Fischer Scientific FS-28) in ice-cold water for 30 min. This led to the cell lysis and the extraction of cellular thiols. The thiols were reduced, tagged with bimanine by reacting with excessive amount of monobromobimane at pH 9. The reaction was terminated upon acidification with methanesulfonic acid solution. The thiol-bimane adduct was analyzed by HPLC with fluorescence detector following a

previously published method (Wei et al. 2010). The quantified glutathione was further normalized to chl a.

MINITAB 16 was used for statistical analysis. One way analysis of variance (ANOVA) was used to compare the effect of different treatment with probability $p < 0.05$ being accepted as statistically significant.

6.7 Results

The pristine single walled carbon nanotubes had a length of 5-30 μm and outer diameter of 1.1 nm. Figure 6.1 shows the Scanning Electron Microscopy (SEM) images of the SWCNTs used in this study; f-SWCNT-A (1a) and f-SWCNT-B (1b) showed similar tubular structures. As expected, carbon black sample (1c) did not show the presence of any tubes.

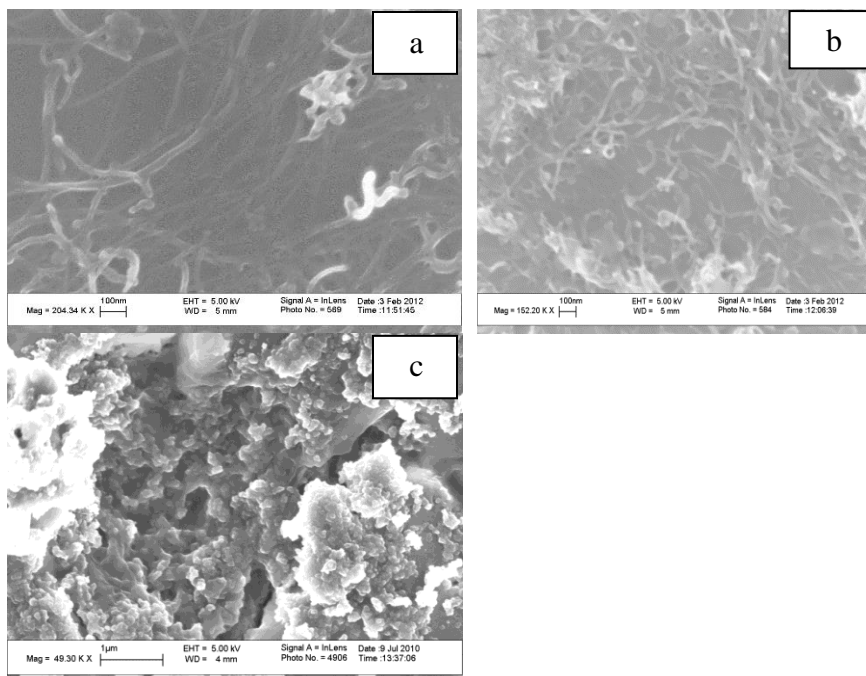


Figure 6. 1 Scanning Electron Microscopy images of: (a) f-SWCNT-A; (b) f-SWCNT-B and (c) Carbon black.

6.7.1 Effect of SWCNTs on Algal Growth

Exponentially growing *D. tertiolecta* cells were inoculated into the pre-equilibrated media containing 0 to 20 mg/L of the sample to be studied.

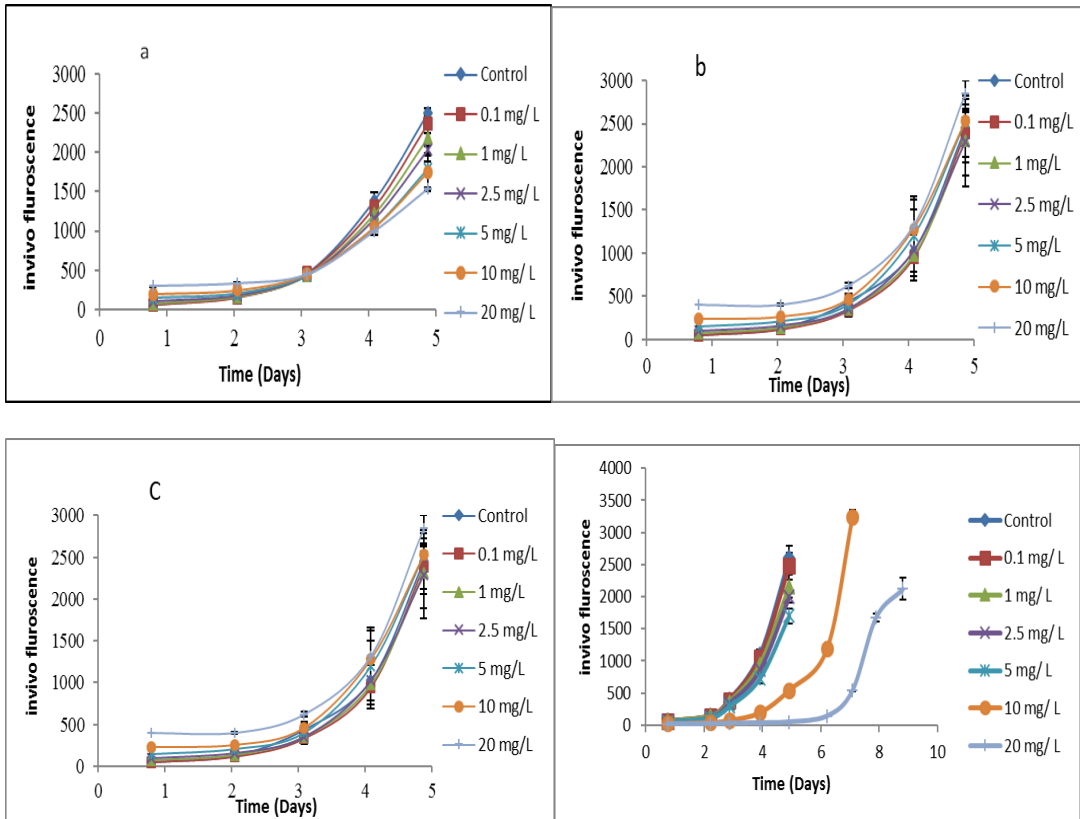


Figure 6.2 *In vivo* chlorophyll a fluorescence based growth curves of *D. tertiolecta* exposed to 0, 0.1, 1, 2.5, 5, 10 and 20 mg/L of samples: (a) f-SWCNT-A; (b) filtrate; (c) f-SWCNT-B, and (d) carbon black.

The resulting growth curves are shown in (Figure 6.2). It is seen that increasing f-SWCNT concentration resulted in increased growth inhibition. When alga was exposed to 10 and 20 mg/L of carbon black it showed a lag phase of 3 days and 4 days, respectively. Cells exposed to the two SWCNTs didn't show any lag phase. The SWCNT

was quite different from what was observed with MWCNT with the same alga (Wei et al. 2010), which showed a 23 day lag phase at CNT concentration of 10 mg/L.

Table 6.1 Inhibition in Growth Rate

Material	Concentration (mg/L)	% inhibition
f-SWCNT-A	5	17±1.5
	10	22±3.9
	20	27±2.4
f-SWCNT- filtrate	20	12±2.4
f-SWCNT-B	5	18±2.8
	10	29±5.0
	20	32±6.0

ANOVA analysis of the growth rate data is presented in Table 6.1. Exposure to Carbon Black didn't show any significant growth rate inhibition. On the other hand, both the f-SWCNTs showed significant growth inhibition. Based on 2 sample t test on exponential growth rate, there was no difference between f-SWCNT-A and f-SWCNT-B. However, there was a significant difference between f-SWCNT-A and the filtrate where the nanotube aggregates had been removed. The filtrate containing only the highly dispersed nanotubes showed growth inhibition only at high concentration (20 mg/L). Thus removal of aggregates by filtration decreased the growth rate inhibition and reduced

toxicity. In the present study, exposure to 10 mg/L of carbon black showed no effect on exponential growth rate and exposure to 10 mg/L f-SWCNT-A and f-SWCNT-B showed exponential growth rate inhibition of $22 \pm 3.9\%$ and $29 \pm 5\%$, respectively. On a comparative basis, our previous study (Wei et al. 2010) with f-MWCNTs had shown a growth rate inhibition of 36% at a concentration of 10 mg/L. Other studies using SWCNT and DWCNT using fresh water algae have shown inhibition as high as 40 to 52% [146, 149].

6.7.2 Aggregation in Presence of SWCNT

Dynamic light scattering (DLS) was used to measure the particle size of the pure nanocarbons in deionized as well as sea water. Concentration of 20 mg/L of Carbon black, f-SWCNT-A and f-SWCNT-B were prepared in MQ and artificial sea water (SOW) to measure particle size and zeta potential. Samples prepared in MQ had a polydispersity of < 0.5 , average size of carbon black was 91 ± 1 nm, f-SWCNT-A was 114.5 ± 9 nm and f-SWCNT-B was 165.5 ± 4 nm. Zeta potential of SWCNT was measured by diluting the stock solution to 5 mg/L with MQ and SOW. Both f-SWCNT-A and f-SWCNT-B were stable in MQ with zeta potential of -39.4 mV and -33.4 mV respectively.

When the suspension was prepared in SOW, the nanotubes were unstable due to aggregation and had a zeta potential of -8.4 mV and -7.4 mV for f-SWCNT-A and f-SWCNT-B, respectively. High concentrations of cationic ions Ca^{2+} , Mg^{2+} , Na^{2+} in seawater are known to destabilize carboxylated CNT suspension by compressing the electrical double layer (Handy et. al 2008). Carbon black had an average size of 473 ± 67

nm, f-SWCNT-A and f-SWCNT-B showed similar tri modal size distribution with peaks around 100, 450 and 750 nm.

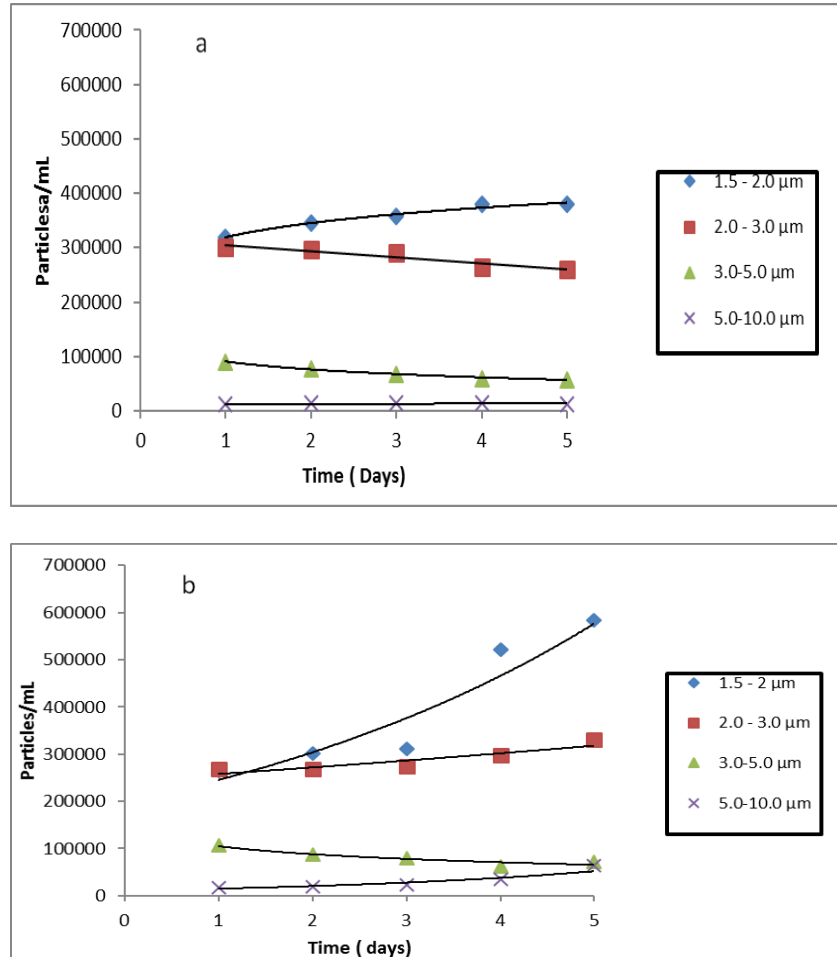


Figure 6.3 Particle size measurements using Multisizer coulter counter; (a) f-SWCNT-B without algae; (b) f-SWCNT-B and algae.

Particle in presence of nanocarbons and algae was monitored using the coulter counter. The f-SWCNT-B exposed cells were monitored daily using 70 μm aperture tube and particles in the range of 1.7 to 10 μm were quantified. Number of particles at different size ranges, 1.7–2, 2-3, 3-5 and 5-10 μm were monitored, these are shown in Figure 7.3a and 7.3b. *D. tertiolecta* represented size range of 5.2 – 9.6 μm, and the

nanocarbons represented the smaller diameters. It was seen that the smaller particles were more abundant. Figure 3 a represents the nanocarbon blank without the alga. It is seen that the particles in the different size ranges did not change significantly with time; the particles between 1.7–2, 2-3, 3-5 and 5-10 μm increased by 19, 14, 36 and 3 %, respectively. On the other hand, in presence of algae (Figure 7.3b) the corresponding changes for the same size ranges were 121, 24, 31 and 259%, respectively. The increase in concentration of the small particle in presence of the alga is attributed to organic matter secreted from algal cells which led to further aggregation. Similar results were observed in our previous study with exposure to f- MWCNT [153] and more recently by Fabienne et al. 2011.

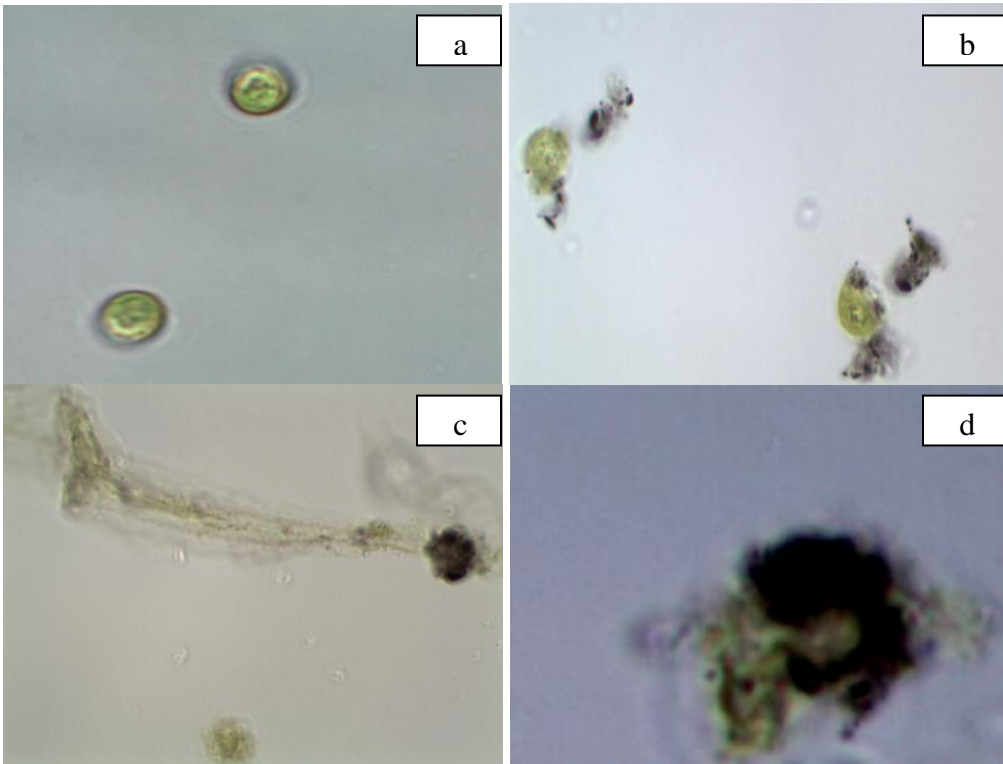


Figure 6.4 Light microscopy of: (a) *D. tertiolecta*; (b-d) different cell aggregated with f-SWCNT-B.

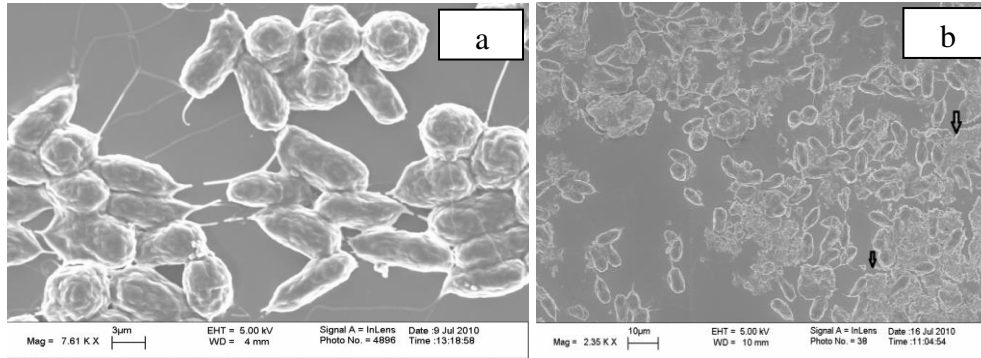


Figure 6.5 Scanning electron microscopic images of: (a) *D. tertiolecta*; (b) cells exposed to f-SWCNT-B showing nanotube aggregates on cell surface.

Physical interactions of f-SWCNT-B with alga were also directly observed using optical microscopy and scanning electron microscopy (Figures 6.4 and 6.5). Light microscopy showed presence of active cells with SWCNT aggregates on the surface and non motile cell entrapped in layers of agglomerated SWCNT. Some cells had also lost cellular integrity and exhibited cytoplasm leakage. Study of Single walled carbon nanotubes on *E. coli* has shown damage of cell membrane and leakage of intracellular matter [157]. Scanning electron microscopy shown in Figure 6.5 also showed the presence of SWCNT aggregates on cell surface.

6.7.3 Photosynthesis

Photosynthesis was monitored by Fluorescence Induction and relaxation system (FIRe). Various induction (f_v/f_m , Sigma, p) and relaxation (Alp1, Alp2, Alp3, Tavav1, Tavav2, Tav3) parameters were studied and analyzed by one way ANOVA with Huckles test as published previously [153].

Table 6.2 Induction and Relaxation Parameters of Photosynthesis of Cells Exposed to 0-20 mg/L of f-SWCNT-A, f- SWCNT filtrate, f-SWCNT-B and Carbon Black

*NA implies not affected

Material	Fv/fm	Sigma	P	Alp1	Tau1	Alp2	Tau2	Tau3	TauAV1	TauAV2
f-SWCNT-A	5,10,20	2.5,5,10,20	5,10,20	NA	NA	NA	NA	NA	NA	10,20
f-SWCNT filtrate	5,10,20	NA	NA	NA	NA	NA	NA	NA	NA	NA
f-SWCNT-B	2.5,5,10,20	1,2.5,5,10	NA	20	NA	20	2.5,5,10,20	2.5,5,10,20	5, 20	2.5,10,20

The study was carried out in the exponential phase and the results are presented in Table 6.2. Cells exposed to f-SWCNT-B showed significant effect on induction parameters such as photosynthetic quantum yield (fv/fm), Sigma, p value and TavAV2 (Table 6.2). The quantum yield decreased by 18% at concentration 20 mg/L. The PSII cross section and Connectivity factor p were reduced by 12 and 21% at 10 and 20 mg/L, respectively. The latter defines the energy transfer between individual PSII units. Increase of Tav-av2 by 114 and 116%, respectively at 10 and 20 mg/L indicated the presence of small fraction of inactive PSII reaction centers that were incapable of fast electron capture. For cells exposed to filtrate without SWCNT aggregates showed reduction in quantum yield by 22% at 20 mg/L. The photosynthetic effects for f-SWCNT-B were more or less similar but there were some differences. These are shown in Table 6.2. The quantum yield decreased by as much as 11%. The results indicate that the presence of f-SWCNT-A affected mainly induction parameters while f-SWCNT-B affected the relaxation parameters as well. In our previous study related to the exposure of MWCNT to the same algae showed similar effect on different photosynthetic

parameters [153] and this is in line with other studies using fresh water algae (Matorin et al. 2010).

6.7.4 Oxidative Stress

The source of oxidative stress has been debated. Reactive oxygen species (ROS) production and subsequent damage of cellular components have often been considered as the cause of oxidative stress (Li et al., 2008) which others have put forward non ROS related mechanisms (Kang et al., 2008; Lyon and Alvarez, 2008).

Many studies have reported oxidative stress as one of the mechanism for toxicity in different types of algae (Long et al. 2012, Wei et al. 2010, Lyon and Alvarez 2008, Kang et al. 2008).

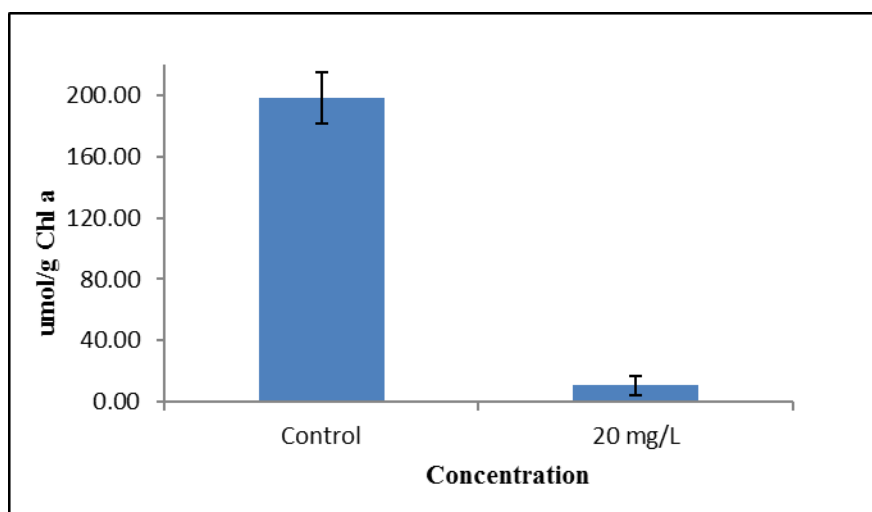


Figure 6.6 Glutathione quantification of *D. tertiolecta* and cells exposed to 20 mg/L of f-SWCNT-B

After 120 hrs exposure with 20 mg/L f-SWCNT-B, the cells were harvested for glutathione quantification (Figure 6.6). Compared to the control, exposed cells showed $95 \pm 3\%$ decrease in total glutathione level when normalized to μ moles of Chl a. This was a

clear indication of oxidative stress and the absolute value is similar to what was reported before for MWCNTs using the same alga [153].

6.8 Conclusion

It is concluded that f-SWCNTs can induce growth inhibition, cause harm to photosynthetic system and adversely affect cellular glutathione levels in *D. tertiolecta*. Majority of the toxicity was attributed to the aggregates of f-SWCNT. Removal of aggregates by filtration decreased the toxicity effects. Exposure to 10 mg/L of f-SWCNTs didn't show lag phase, whereas Carbon black showed a lag phase of 3 days. On comparative basis our previous studies with f-MWCNT had shown a lag phase of 23 days implying that the SWCNTs behave differently from MWCNTs. The photosynthetic activity was comparable to what we had observed with MWCNTs. The presence of SWCNTs also showed a 95% inhibition in intracellular glutathione concentrations.

REFERENCES

1. Round, F.E., R.M. Crawford, and D.G. Mann, *The diatoms: biology & morphology of the genera*. 1990: Cambridge University Press.
2. Hamm, C.E., et al., *Architecture and material properties of diatom shells provide effective mechanical protection*. *Nature*, 2003. **421**(6925): p. 841-843.
3. Losic, D., et al., *Controlled pore structure modification of diatoms by atomic layer deposition of TiO₂*. *Journal of Materials Chemistry*, 2006. **16**(41): p. 4029-4034.
4. Wang, Y., et al., *Preparation of biosilica structures from frustules of diatoms and their applications: current state and perspectives*. *Applied Microbiology and Biotechnology*, 2013. **97**(2): p. 453-460.
5. Losic, D., et al., *Pore architecture of diatom frustules: potential nanostructured membranes for molecular and particle separations*. *Journal of Nanoscience and Nanotechnology*, 2006. **6**(4): p. 982-989.
6. Bao, Z., et al., *Chemical reduction of three-dimensional silica micro-assemblies into microporous silicon replicas*. *Nature*, 2007. **446**(7132): p. 172-175.
7. Jeffryes, C., et al., *The potential of diatom nanobiotechnology for applications in solar cells, batteries, and electroluminescent devices*. *Energy & Environmental Science*, 2011. **4**(10): p. 3930-3941.
8. Wang, Y., et al., *Key factors influencing the optical detection of biomolecules by their evaporative assembly on diatom frustules*. *Journal of Materials Science*, 2012. **47**(17): p. 6315-6325.
9. Aw, M.S., et al., *Porous silica microshells from diatoms as biocarrier for drug delivery applications*. *Powder technology*, 2012. **223**: p. 52-58.
10. Gélabert, A., et al., *Study of diatoms/aqueous solution interface. I. Acid-base equilibria and spectroscopic observation of freshwater and marine species*. *Geochimica et Cosmochimica Acta*, 2004. **68**(20): p. 4039-4058.
11. Gélabert, A., et al., *Cadmium and lead interaction with diatom surfaces: A combined thermodynamic and kinetic approach*. *Geochimica et Cosmochimica Acta*, 2007. **71**(15): p. 3698-3716.

12. Zhao, X., et al., *Polymer-supported nanocomposites for environmental application: A review*. Chemical Engineering Journal, 2011. **170**(2–3): p. 381-394.
13. Atieh, M.A., *Removal of Chromium (VI) from polluted water using carbon nanotubes supported with activated carbon*. Procedia Environmental Sciences, 2011. **4**(0): p. 281-293.
14. Sinha Ray, S., et al., *New Polylactide/Layered Silicate Nanocomposites. 3. High-Performance Biodegradable Materials*. Chemistry of Materials, 2003. **15**(7): p. 1456-1465.
15. Ferroudj, N., et al., *Maghemite nanoparticles and maghemite/silica nanocomposite microspheres as magnetic Fenton catalysts for the removal of water pollutants*. Applied Catalysis B: Environmental, 2013. **136–137**(0): p. 9-18.
16. Kokate, M., K. Garadkar, and A. Gole, *One pot synthesis of magnetite-silica nanocomposites: Applications as tags, entrapment matrix and in water purification*. Journal of Materials Chemistry A, 2013. **1**(6): p. 2022-2029.
17. Caparrós, C., et al., *Hydrothermal assisted synthesis of iron oxide-based magnetic silica spheres and their performance in magnetophoretic water purification*. Materials Chemistry and Physics, 2012. **135**(2-3): p. 510-517.
18. Yu, X., et al., *One-step synthesis of magnetic composites of cellulose@iron oxide nanoparticles for arsenic removal*. Journal of Materials Chemistry A, 2013. **1**(3): p. 959-965.
19. Liu, Z., et al., *Magnetic cellulose-chitosan hydrogels prepared from ionic liquids as reusable adsorbent for removal of heavy metal ions*. Chemical Communications, 2012. **48**(59): p. 7350-7352.
20. Zhou, Y.T., et al., *Removal of Cu²⁺ from aqueous solution by chitosan-coated magnetic nanoparticles modified with α -ketoglutaric acid*. Journal of Colloid and Interface Science, 2009. **330**(1): p. 29-37.
21. Chang, Y.C. and D.H. Chen, *Preparation and adsorption properties of monodisperse chitosan-bound Fe₃O₄ magnetic nanoparticles for removal of Cu(II) ions*. Journal of Colloid and Interface Science, 2005. **283**(2): p. 446-451.
22. Hansen, B.Ø., et al., *Use of iron oxide-coated sand to remove strontium from simulated Hanford tank wastes*. Environmental Science and Technology, 2001. **35**(24): p. 4905-4909.
23. Ding, C., et al., *Removal of natural organic matter using surfactant-modified iron oxide-coated sand*. Journal of Hazardous Materials, 2010. **174**(1-3): p. 567-572.

24. Ge, F., et al., *Effective removal of heavy metal ions Cd²⁺, Zn²⁺, Pb²⁺, Cu²⁺ from aqueous solution by polymer-modified magnetic nanoparticles*. Journal of Hazardous Materials, 2012. **211–212**(0): p. 366-372.
25. Badruddoza, A.Z.M., et al., *Fe₃O₄/cyclodextrin polymer nanocomposites for selective heavy metals removal from industrial wastewater*. Carbohydrate Polymers, 2013. **91**(1): p. 322-332.
26. Farrukh, A., et al., *Design of Polymer-Brush-Grafted Magnetic Nanoparticles for Highly Efficient Water Remediation*. ACS Applied Materials & Interfaces, 2013. **5**(9): p. 3784-3793.
27. Addo Ntim, S. and S. Mitra, *Removal of Trace Arsenic To Meet Drinking Water Standards Using Iron Oxide Coated Multiwall Carbon Nanotubes*. Journal of Chemical & Engineering Data, 2011. **56**(5): p. 2077-2083.
28. Addo Ntim, S. and S. Mitra, *Adsorption of arsenic on multiwall carbon nanotube–zirconia nanohybrid for potential drinking water purification*. Journal of Colloid and Interface Science, 2012. **375**(1): p. 154-159.
29. Gupta, V.K., S. Agarwal, and T.A. Saleh, *Synthesis and characterization of alumina-coated carbon nanotubes and their application for lead removal*. Journal of Hazardous Materials, 2011. **185**(1): p. 17-23.
30. Yang, S., et al., *Application of a novel plasma-induced CD/MWCNT/iron oxide composite in zinc decontamination*. Carbohydrate Polymers, 2012. **90**(2): p. 1100-1105.
31. Sciences, T.N.A.o., *Fluoride in drinking water*. 2006.
32. Bhatnagar, A., E. Kumar, and M. Sillanpää, *Fluoride removal from water by adsorption—A review*. Chemical Engineering Journal, 2011. **171**(3): p. 811-840.
33. USNRC, *Fluoride in Drinking Water: A Scientific Review of EPA's Standards*. . Committee on Fluoride in Drinking Water, National Research Council 2006. **ISBN: 0-309-65796-2**: p. 532.
34. *Fluoride in New Jersey Public Water Supplies Report*. NJDEP, January 2011
35. Loganathan, P., et al., *Defluoridation of drinking water using adsorption processes*. Journal of Hazardous Materials, 2013. **248-249**(1): p. 1-19.
36. Pan, B., et al., *Enhanced removal of fluoride by polystyrene anion exchanger supported hydrous zirconium oxide nanoparticles*. Environmental Science and Technology, 2013. **47**(16): p. 9347-9354.

37. Sai Sathish Ramamurthy, Y.C., M. Kamesh Kalyan, G. Nageswara Rao, Janardhana Chelli, and Somenath Mitra, *Carbon Nanotube-Zirconium Dioxide Hybrid for Defluoridation of Water*. Journal of Nanoscience and Nanotechnology, 2011. **11**: p. 1-8.
38. Price, N.M., et al., *Preparation and chemistry of the artificial algal culture medium Aquil*. Biological Oceanography, 1989. **6**(5-6): p. 443-461.
39. Wang, J.A., et al., *Surfactant-assisted synthesis of defective zirconia mesophases and Pd/ZrO₂: Crystalline structure and catalytic properties*. Applied Surface Science, 2008. **254**(16): p. 5061-5072.
40. Du, J., et al., *Understanding the toxicity of carbon nanotubes in the environment is crucial to the control of nanomaterials in producing and processing and the assessment of health risk for human: A review*. Environmental Toxicology and Pharmacology, 2013. **36**(2): p. 451-462.
41. Matorin, D., et al., *Influence of carbon nanotubes on chlorophyll fluorescence parameters of green algae Chlamydomonas reinhardtii*. Nanotechnologies in Russia, 2010. **5**(5-6): p. 320-327.
42. Zhang, L., et al., *Effect of natural and synthetic surface coatings on the toxicity of multiwalled carbon nanotubes toward green algae*. Carbon, 2015. **83**: p. 198-207.
43. Gao, Y., et al., *Formulation optimization and in situ absorption in rat intestinal tract of quercetin-loaded microemulsion*. Colloids and Surfaces B: Biointerfaces, 2009. **71**(2): p. 306-314.
44. Al-Hamidi, H., et al., *Glucosamine HCl as a new carrier for improved dissolution behaviour: Effect of grinding*. Colloids and Surfaces B: Biointerfaces, 2010. **81**(1): p. 96-109.
45. Xia, D., et al., *Preparation of stable nitrendipine nanosuspensions using the precipitation-ultrasonication method for enhancement of dissolution and oral bioavailability*. European Journal of Pharmaceutical Sciences, 2010. **40**(4): p. 325-334.
46. Lonare, A.A. and S.R. Patel, *Antisolvent crystallization of poorly water soluble drugs*. International Journal of Chemical Engineering and Applications, 2013. **4**(5): p. 337.
47. Veiga, M.D., P.J. Díaz, and F. Ahsan, *Interactions of griseofulvin with cyclodextrins in solid binary systems*. Journal of pharmaceutical sciences, 1998. **87**(7): p. 891-900.

48. Aggarwal, N., S. Goindi, and R. Khurana, *Formulation, characterization and evaluation of an optimized microemulsion formulation of griseofulvin for topical application*. Colloids and Surfaces B: Biointerfaces, 2013. **105**: p. 158-166.
49. Dong, W. and R. Bodmeier, *Encapsulation of lipophilic drugs within enteric microparticles by a novel coacervation method*. International journal of pharmaceutics, 2006. **326**(1): p. 128-138.
50. Aggarwal, N. and S. Goindi, *Preparation and evaluation of antifungal efficacy of griseofulvin loaded deformable membrane vesicles in optimized guinea pig model of *Microsporum canis*—Dermatophytosis*. International Journal of Pharmaceutics, 2012. **437**(1–2): p. 277-287.
51. Suh, Y.W. and H.K. Rhee, *Synthesis, characterization and catalytic application of mesoporous sulfated zirconia*, in *Studies in Surface Science and Catalysis*. 2002. p. 289-296.
52. Van Wambeke, F., *Fate of *Phaeodactylum tricornutum* and nitrogen flow in an experimental microbial food web limited at the top by protozoans*. Aquatic microbial ecology, 1995. **9**(2): p. 127-136.
53. Singh, A. and U.T. Nakate, *Microwave synthesis, characterization, and photoluminescence properties of nanocrystalline zirconia*. The Scientific World Journal, 2014. **2014**.
54. Jere, G.V. and M.T. Santhamma, *IR and laser raman studies on peroxo fluoro species of zirconium*. Inorganica Chimica Acta, 1977. **24**(0): p. 57-61.
55. Dalagan, J.Q. and E.P. Enriquez, *Interaction of Diatom Silica with Graphene*. Phillipine Science Letters, 2013. **6**(1): p. 119-127.
56. Guan, M., et al., *Preparation, characterization and adsorption properties studies of 3-(methacryloyloxy)propyltrimethoxysilane modified and polymerized sol–gel mesoporous SBA-15 silica molecular sieves*. Microporous and Mesoporous Materials, 2009. **123**(1–3): p. 193-201.
57. Möller, K., J. Kobler, and T. Bein, *Colloidal suspensions of nanometer-sized mesoporous silica*. Advanced Functional Materials, 2007. **17**(4): p. 605-612.
58. Kao, H.-M., et al., *Control of ordered structure and morphology of cubic mesoporous silica SBA-1 via direct synthesis of thiol-functionalization*. Microporous and Mesoporous Materials, 2008. **110**(2): p. 461-471.
59. Lagergren, S., *About the theory of so-called adsorption of soluble substances*. Kungliga Svenska Vetenskapsakademiens Handlingar, 1898. **24**(4): p. 1-39.

60. Ho, Y.-S. and G. McKay, *The kinetics of sorption of divalent metal ions onto sphagnum moss peat*. Water Research, 2000. **34**(3): p. 735-742.
61. Yuh-Shan, H., *Citation review of Lagergren kinetic rate equation on adsorption reactions*. Scientometrics, 2004. **59**(1): p. 171-177.
62. Bulut, E., M. Özacar, and İ.A. Şengil, *Adsorption of malachite green onto bentonite: Equilibrium and kinetic studies and process design*. Microporous and Mesoporous Materials, 2008. **115**(3): p. 234-246.
63. Barathi, M., A.S.K. Kumar, and N. Rajesh, *A novel ultrasonication method in the preparation of zirconium impregnated cellulose for effective fluoride adsorption*. Ultrasonics Sonochemistry, 2014. **21**(3): p. 1090-1099.
64. Ramamurthy, S.S., et al., *Carbon Nanotube-Zirconium Dioxide Hybrid for Defluoridation of Water*. Journal of Nanoscience and Nanotechnology, 2011. **11**(4): p. 3552-3559.
65. Langmuir, I., *THE ADSORPTION OF GASES ON PLANE SURFACES OF GLASS, MICA AND PLATINUM*. Journal of the American Chemical Society, 1918. **40**(9): p. 1361-1403.
66. Freundlich, H., *Over the adsorption in solution*. J. Phys. Chem, 1906. **57**(385471): p. 1100-1107.
67. Hall, K.R., et al., *Pore- and Solid-Diffusion Kinetics in Fixed-Bed Adsorption under Constant-Pattern Conditions*. Industrial & Engineering Chemistry Fundamentals, 1966. **5**(2): p. 212-223.
68. Malik, P., *Dye removal from wastewater using activated carbon developed from sawdust: adsorption equilibrium and kinetics*. Journal of Hazardous Materials, 2004. **113**(1): p. 81-88.
69. Poots, V., G. McKay, and J. Healy, *Removal of basic dye from effluent using wood as an adsorbent*. Journal (Water Pollution Control Federation), 1978: p. 926-935.
70. Zhang, Q., et al., *Rationally designed porous polystyrene encapsulated zirconium phosphate nanocomposite for highly efficient fluoride uptake in waters*. Scientific reports, 2013. **3**.
71. Dou, X., et al., *Remediating fluoride from water using hydrous zirconium oxide*. Chemical Engineering Journal, 2012. **198**: p. 236-245.

72. He, J. and J.P. Chen, *A zirconium-based nanoparticle: Essential factors for sustainable application in treatment of fluoride containing water*. Journal of Colloid and Interface Science, 2014. **416**: p. 227-234.
73. Mohan, D. and C.U. Pittman Jr, *Arsenic removal from water/wastewater using adsorbents—A critical review*. Journal of Hazardous Materials, 2007. **142**(1–2): p. 1-53.
74. Chatterjee, A., et al., *Arsenic in ground water in six districts of West Bengal, India: the biggest arsenic calamity in the world. Part I. Arsenic species in drinking water and urine of the affected people*. Analyst, 1995. **120**(3): p. 643-650.
75. Mondal, P., C.B. Majumder, and B. Mohanty, *Laboratory based approaches for arsenic remediation from contaminated water: Recent developments*. Journal of Hazardous Materials, 2006. **137**(1): p. 464-479.
76. Chowdhury, U.K., et al., *Groundwater arsenic contamination in Bangladesh and West Bengal, India*. Environmental health perspectives, 2000. **108**(5): p. 393.
77. Mandal, B.K. and K.T. Suzuki, *Arsenic round the world: a review*. Talanta, 2002. **58**(1): p. 201-235.
78. Spayd, S.E., *Arsenic Water Treatment for Residential Wells in New Jersey*. 2007.
79. Knowles, F.C. and A.A. Benson, *The biochemistry of arsenic*. Trends in Biochemical Sciences, 1983. **8**(5): p. 178-180.
80. Pattanayak, J., et al., *A parametric evaluation of the removal of As(V) and As(III) by carbon-based adsorbents*. Carbon, 2000. **38**(4): p. 589-596.
81. Giles, D.E., et al., *Iron and aluminium based adsorption strategies for removing arsenic from water*. Journal of Environmental Management, 2011. **92**(12): p. 3011-3022.
82. Baolin, D., C. Mendy, and G. Zhimang, *Arsenic Removal by Activated Carbon-Based Materials*, in *Advances in Arsenic Research*. 2005, American Chemical Society. p. 284-293.
83. Zeng, L., *A method for preparing silica-containing iron(III) oxide adsorbents for arsenic removal*. Water Research, 2003. **37**(18): p. 4351-4358.
84. Swedlund, P.J. and J.G. Webster, *Adsorption and polymerisation of silicic acid on ferrihydrite, and its effect on arsenic adsorption*. Water Research, 1999. **33**(16): p. 3413-3422.

85. Herbillon, A.J. and J.T. Vinh An, *Heterogeneity in Silicon-Iron Mixed hydroxides* Journal of Soil Science, 1969. **20**(2): p. 223-235.
86. Dalagan, J.Q. and E.P. Enriquez, *Interaction of Diatom Silica with Graphene*.
87. Ullah, R., B.K. Deb, and M.Y.A. Mollah, *Synthesis and Characterization of Silica Coated Iron-Oxide Composites of Different Ratios*. International Journal of Composite Materials, 2014. **4**(2): p. 135-145.
88. Guan, M., et al., *Preparation, characterization and adsorption properties studies of 3-(methacryloyloxy)propyltrimethoxysilane modified and polymerized sol-gel mesoporous SBA-15 silica molecular sieves*. Microporous and Mesoporous Materials, 2009. **123**(1-3): p. 193-201.
89. Möller, K., J. Kobler, and T. Bein, *Colloidal suspensions of nanometer-sized mesoporous silica*. Advanced Functional Materials, 2007. **17**(4): p. 605-612.
90. Kao, H.M., et al., *Control of ordered structure and morphology of cubic mesoporous silica SBA-1 via direct synthesis of thiol-functionalization*. Microporous and Mesoporous Materials, 2008. **110**(2-3): p. 461-471.
91. Banerjee, K., et al., *Kinetic and thermodynamic aspects of adsorption of arsenic onto granular ferric hydroxide (GFH)*. Water Research, 2008. **42**(13): p. 3371-3378.
92. Raven, K.P., A. Jain, and R.H. Loeppert, *Arsenite and Arsenate Adsorption on Ferrihydrite: Kinetics, Equilibrium, and Adsorption Envelopes*. Environmental Science & Technology, 1998. **32**(3): p. 344-349.
93. Thakkar, M., et al., *Water defluoridation using a nanostructured diatom–ZrO₂ composite synthesized from algal Biomass*. Journal of Colloid and Interface Science, 2015. **450**(0): p. 239-245.
94. Ho, Y.S. and G. McKay, *The kinetics of sorption of divalent metal ions onto sphagnum moss peat*. Water Research, 2000. **34**(3): p. 735-742.
95. Sharma, S., R. Singh, and G.G. Nielson, *Selenium in soil, plant, and animal systems*. Critical Reviews in Environmental Science and Technology, 1983. **13**(1): p. 23-50.
96. Ohlendorf, H.M., *Bioaccumulation and effects of selenium in wildlife*. Selenium in Agriculture and the Environment, 1989(seleniuminagric): p. 133-177.
97. Strawn, D., et al., *Microscale investigation into the geochemistry of arsenic, selenium, and iron in soil developed in pyritic shale materials*. Geoderma, 2002. **108**(3): p. 237-257.

98. Gonzalez, C.M., et al., *Sorption kinetic study of selenite and selenate onto a high and low pressure aged iron oxide nanomaterial*. Journal of Hazardous Materials, 2012. **211–212**: p. 138-145.
99. Fernandez, M.G.C., M.A. Palacios, and C. Camara, *Flow-injection and continuous-flow systems for the determination of Se(IV) and Se(VI) by hydride generation atomic absorption spectrometry with on-line prereduction of Se(VI) to Se(IV)*. Analytica Chimica Acta, 1993. **283**(1): p. 386-392.
100. Santos, S., et al., *Selenium contaminated waters: an overview of analytical methods, treatment options and recent advances in sorption methods*. Science of The Total Environment, 2015. **521**: p. 246-260.
101. Frankenberger, W.T. and M. Arshad, *Bioremediation of selenium-contaminated sediments and water*. Biofactors, 2001. **14**(1-4): p. 241-254.
102. Mavrov, V., et al., *New hybrid electrocoagulation membrane process for removing selenium from industrial wastewater*. Desalination, 2006. **201**(1): p. 290-296.
103. El-Shafey, E., *Removal of Se (IV) from aqueous solution using sulphuric acid-treated peanut shell*. Journal of Environmental Management, 2007. **84**(4): p. 620-627.
104. Sharrad, M.O.M., H. Liu, and M. Fan, *Evaluation of FeOOH performance on selenium reduction*. Separation and Purification Technology, 2012. **84**: p. 29-34.
105. Duc, M., G. Lefèvre, and M. Fédoroff, *Sorption of selenite ions on hematite*. Journal of Colloid and Interface Science, 2006. **298**(2): p. 556-563.
106. Das, J., et al., *Studies on Mg/Fe hydrotalcite-like-compound (HTlc): I. Removal of inorganic selenite (SeO₃²⁻) from aqueous medium*. Journal of Colloid and Interface Science, 2002. **251**(1): p. 26-32.
107. Martínez, M., et al., *Sorption of selenium(IV) and selenium(VI) onto magnetite*. Applied Surface Science, 2006. **252**(10): p. 3767-3773.
108. Zhang, N., L.S. Lin, and D. Gang, *Adsorptive selenite removal from water using iron-coated GAC adsorbents*. Water Research, 2008. **42**(14): p. 3809-3816.
109. Gonzalez, C.M., et al., *A study of the removal of selenite and selenate from aqueous solutions using a magnetic iron/manganese oxide nanomaterial and ICP-MS*. Microchemical Journal, 2010. **96**(2): p. 324-329.

110. Zhang, M. and E.J. Reardon, *Removal of B, Cr, Mo, and Se from wastewater by incorporation into hydrocalumite and ettringite*. Environmental science & technology, 2003. **37**(13): p. 2947-2952.
111. Roussel, T., C. Bichara, and R.J.-M. Pellenq, *Selenium and carbon nanostructures in the pores of AlPO₄-5*. Adsorption, 2005. **11**(1): p. 709-714.
112. Ippolito, J.A., K.G. Scheckel, and K.A. Barbarick, *Selenium adsorption to aluminum-based water treatment residuals*. Journal of colloid and interface science, 2009. **338**(1): p. 48-55.
113. Bonhoure, I., et al., *Uptake of Se (IV/VI) oxyanions by hardened cement paste and cement minerals: an X-ray absorption spectroscopy study*. Cement and Concrete Research, 2006. **36**(1): p. 91-98.
114. Peak, D., *Adsorption mechanisms of selenium oxyanions at the aluminum oxide/water interface*. Journal of colloid and interface science, 2006. **303**(2): p. 337-345.
115. Parida, K., et al., *Studies on ferric oxide hydroxides: III. Adsorption of selenite (SeO₂- 3) on different forms of iron oxyhydroxides*. Journal of colloid and interface science, 1997. **185**(2): p. 355-362.
116. Lo, S.-L. and T.-Y. Chen, *Adsorption of Se (IV) and Se (VI) on an iron-coated sand from water*. Chemosphere, 1997. **35**(5): p. 919-930.
117. Zhang, Y., et al., *Removal of selenate from water by zerovalent iron*. Journal of environmental quality, 2005. **34**(2): p. 487-495.
118. Chubar, N., *New inorganic (an)ion exchangers based on Mg-Al hydrous oxides: (Alkoxide-free) sol-gel synthesis and characterisation*. Journal of Colloid and Interface Science, 2011. **357**(1): p. 198-209.
119. Szlachta, M., V. Gerda, and N. Chubar, *Adsorption of arsenite and selenite using an inorganic ion exchanger based on Fe-Mn hydrous oxide*. Journal of Colloid and Interface Science, 2012. **365**(1): p. 213-221.
120. Suzuki, T.M., et al., *Adsorption characteristics and removal of oxo-anions of arsenic and selenium on the porous polymers loaded with monoclinic hydrous zirconium oxide*. Separation Science and Technology, 2001. **36**(1): p. 103-111.
121. Szlachta, M. and N. Chubar, *The application of Fe-Mn hydrous oxides based adsorbent for removing selenium species from water*. Chemical Engineering Journal, 2013. **217**: p. 159-168.
122. Peak, D. and D. Sparks, *Mechanisms of selenate adsorption on iron oxides and hydroxides*. Environmental Science & Technology, 2002. **36**(7): p. 1460-1466.

123. Tuzen, M. and A. Sari, *Biosorption of selenium from aqueous solution by green algae (Cladophora hutchinsiae) biomass: equilibrium, thermodynamic and kinetic studies*. Chemical Engineering Journal, 2010. **158**(2): p. 200-206.
124. Vallet-Regí, M., F. Balas, and D. Arcos, *Mesoporous materials for drug delivery*. Angewandte Chemie International Edition, 2007. **46**(40): p. 7548-7558.
125. Vallet-Regí, M., *Ordered mesoporous materials in the context of drug delivery systems and bone tissue engineering*. Chemistry—A European Journal, 2006. **12**(23): p. 5934-5943.
126. Bharti, C., et al., *Mesoporous silica nanoparticles in target drug delivery system: a review*. International journal of pharmaceutical investigation, 2015. **5**(3): p. 124.
127. Losic, D., et al., *Surface functionalisation of diatoms with dopamine modified iron-oxide nanoparticles: toward magnetically guided drug microcarriers with biologically derived morphologies*. Chemical Communications, 2010. **46**(34): p. 6323-6325.
128. Lopez, P.J., et al., *Prospects in diatom research*. Current Opinion in Biotechnology, 2005. **16**(2): p. 180-186.
129. Losic, D., J.G. Mitchell, and N.H. Voelcker, *Diatomaceous lessons in nanotechnology and advanced materials*. Advanced Materials, 2009. **21**(29): p. 2947-2958.
130. Dolatabadi, J.E.N. and M. de la Guardia, *Applications of diatoms and silica nanotechnology in biosensing, drug and gene delivery, and formation of complex metal nanostructures*. TrAC Trends in Analytical Chemistry, 2011. **30**(9): p. 1538-1548.
131. Sumper, M. and E. Brunner, *Learning from diatoms: nature's tools for the production of nanostructured silica*. Advanced Functional Materials, 2006. **16**(1): p. 17-26.
132. Gnanamoorthy, P., S. Anandhan, and V.A. Prabu, *Natural nanoporous silica frustules from marine diatom as a biocarrier for drug delivery*. Journal of Porous Materials, 2014. **21**(5): p. 789-796.
133. Aggarwal, N. and S. Goindi, *Preparation and evaluation of antifungal efficacy of griseofulvin loaded deformable membrane vesicles in optimized guinea pig model of Microsporum canis—Dermatophytosis*. International Journal of Pharmaceutics, 2012. **437**(1): p. 277-287.

134. Thakkar, M., et al., *Water defluoridation using a nanostructured diatom–ZrO₂ composite synthesized from algal Biomass*. Journal of Colloid and Interface Science, 2015. **450**: p. 239-245.
135. Meng, X., et al., *Stabilizing dispersions of hydrophobic drug molecules using cellulose ethers during anti-solvent synthesis of micro-particulates*. Colloids and Surfaces B: Biointerfaces, 2009. **70**(1): p. 7-14.
136. Thakkar, M., et al., *Water defluoridation using a nanostructured diatom–ZrO₂ composite synthesized from algal Biomass*. Journal of Colloid and Interface Science, 2015. **450**: p. 239-245.
137. Lopez, F.L., et al., *Amorphous formulations of indomethacin and griseofulvin prepared by electrospinning*. Molecular pharmaceutics, 2014. **11**(12): p. 4327-4338.
138. Meng, X., et al., *Synthesis and immobilization of micro-scale drug particles in cellulosic films*. Colloids and Surfaces B: Biointerfaces, 2011. **86**(1): p. 181-188.
139. Schwyzer, I., et al., *Long-term colloidal stability of 10 carbon nanotube types in the absence/presence of humic acid and calcium*. Environmental Pollution, 2012. **169**: p. 64-73.
140. Nowack, B., et al., *Potential release scenarios for carbon nanotubes used in composites*. Environment International, 2013. **59**: p. 1-11.
141. Petersen, E.J. and T.B. Henry, *Methodological considerations for testing the ecotoxicity of carbon nanotubes and fullerenes: Review*. Environmental Toxicology and Chemistry, 2012. **31**(1): p. 60-72.
142. Jackson, P., et al., *Bioaccumulation and ecotoxicity of carbon nanotubes*. Chemistry Central Journal, 2013. **7**(1): p. 1-21.
143. Hou, W.-C., P. Westerhoff, and J.D. Posner, *Biological accumulation of engineered nanomaterials: a review of current knowledge*. Environmental Science: Processes & Impacts, 2013. **15**(1): p. 103-122.
144. Pereira, M.M., et al., *Ecotoxicological effects of carbon nanotubes and cellulose nanofibers in Chlorella vulgaris*. Journal of Nanobiotechnology, 2014. **12**(1).
145. Long, Z., et al., *Systematic and quantitative investigation of the mechanism of carbon nanotubes' toxicity toward Algae*. Environmental Science and Technology, 2012. **46**(15): p. 8458-8466.
146. Sohn, E.K., et al., *Acute toxicity comparison of single-walled carbon nanotubes in various freshwater organisms*. BioMed Research International, 2015. **2015**.

147. Youn, S., et al., *Mitigation of the impact of single-walled carbon nanotubes on a freshwater green algae: Pseudokirchneriella subcapitata*. *Nanotoxicology*, 2012. **6**(2): p. 161-172.
148. Wang, Y. and K. Yang, *Toxicity of single-walled carbon nanotubes on green microalga Chromochloris zofingiensis*. *Chinese Journal of Oceanology and Limnology*, 2013. **31**(2): p. 306-311.
149. Mou, F., et al., *Growth inhibitions of four types of CNTs on Scenedesmus obliquus*. *Journal of Convergence Information Technology*, 2013. **8**(10): p. 176.
150. Jia, G., et al., *Cytotoxicity of Carbon Nanomaterials: Single-Wall Nanotube, Multi-Wall Nanotube, and Fullerene*. *Environmental Science & Technology*, 2005. **39**(5): p. 1378-1383.
151. Basniwal, R.K., et al., *Toxicity study of multiwalled carbon nanotubes on freshwater aquatic algae*. *Journal of Bionanoscience*, 2013. **7**(5): p. 597-600.
152. Clar, J.G., et al., *Unique Toxicological Behavior from Single-Wall Carbon Nanotubes Separated via Selective Adsorption on Hydrogels*. *Environmental Science & Technology*, 2015. **49**(6): p. 3913-3921.
153. Wei, L., et al., *Cytotoxicity effects of water dispersible oxidized multiwalled carbon nanotubes on marine alga, Dunaliella tertiolecta*. *Aquatic Toxicology*, 2010. **100**(2): p. 194-201.
154. Price, N.M., et al., *Preparation and chemistry of the artificial algal culture medium Aquil*. *Biological Oceanography*, 1988/1989. **6**: p. 443-461.
155. Arar, E.J., *Method 446.0 In vitro determination of chlorophyll a, b, c1+c2 and pheopigments in marine and freshwater algae by visible spectrophotometry*. 1997, National Exposure Research Laboratory Office of Research and Development U.S. Environmental Protection Agency: Cincinnati, Ohio 45268.
156. Gorbunov, M.Y. and P.G. Falkowski, *Fluorescence induction and relaxation (FIRe) technique and instrumentation for monitoring photosynthetic processes and primary production in aquatic ecosystems*. "Photosynthesis": Fundamental Aspects to Global Perspectives, ed. a.v.d.E.A.E. Bruce D. 2004, Montreal: Allen Press, . 1029-1031.
157. Kang, S., et al., *Single-walled carbon nanotubes exhibit strong antimicrobial activity*. *Langmuir*, 2007. **23**(17): p. 8670-8673.